Journal of Non-Crystalline Solids 666 (2025) 123682

Contents lists available at ScienceDirect

Journal of Non-Crystalline Solids

journal homepage: www.elsevier.com/locate/jnoncrysol

Molecular dynamics simulation and machine learning to predict mechanical behavior of Cu/Zr multilayer nanofilms under tension-compression

Hoang-Giang Nguyen [a,b,c], Sheng-Joue Young [b], Thanh-Dung Le [d,e], Chi-Ngon Nguyen [f], Le-Binh Do [c], Thai-Nam Nguyen [g], Te-Hua Fang [a,h,*]

[a] Department of Mechanical Engineering, National Kaohsiung University of Science and Technology, Kaohsiung 807, Taiwan
[b] Department of Electronic Engineering, National United University, Miaoli City, Taiwan
[c] Faculty of Engineering, Kien Giang University, Kien Giang Province, Vietnam
[d] Department of Electrical Engineering, Écolede Technologie Supérieure, University of Québec, Montréal, Québec, Canada
[e] Interdisciplinary Centre for Security, Reliability, and Trust (SnT), University of Luxembourg, Luxembourg
[f] College of Engineering, Can Tho University, Ninh Kieu District, 94000 Can Tho, Vietnam
[g] Department of Electronic Engineering, National Kaohsiung University of Science and Technology, Kaohsiung 807, Taiwan
[h] Department of Fragrance and Cosmetic Science, Kaohsiung Medical University, Kaohsiung 807, Taiwan

ARTICLE INFO

Keywords:
Molecular dynamics
Machine learning
Mechanical properties
Multilayer nanofilms

ABSTRACT

This study utilizes molecular dynamics simulations to examine the mechanical response of Cu/Zr multilayer nanofilms under tension and compression deformation with the assistance of machine learning. The results demonstrate slip behavior during the tensile process, occurring exclusively in the Cu film, and phase transformation during the compression process, occurring solely in the Zr film. Additionally, this study investigates the effects of temperature, layer thickness, and strain rate on dislocation evolution within nanofilms. This study reveals that lattice disorder in Cu/Zr nanofilms mitigates the impact of external conditions by inhibiting the reverse movement of dislocations. Temperature and strain rate significantly affect the mechanical behavior, while the number of layers is negligible. Therefore, temperature and strain rate primarily influence plastic deformation in Cu/Zr nanofilms. Additionally, the research elucidates how temperature, strain rates, and layer configuration contribute to lattice disorder. These findings offer novel insights into the mechanical characteristics and deformation mechanisms of Cu/Zr at the atomic scale.

1. Introduction

Multilayer nanofilms (MNFs) have garnered significant interest due to their versatile applications, stemming from the ease with which their production processes can be customized to meet specific performance criteria [1–3]. Recent studies have focused mainly on the nanostructures and electromagnetic properties of MNFs, highlighting their potential in various technological fields [4–7]. Nanoscale metallic multilayers have received global interest in recent years [8–11] and have shown significant promise for various applications, including gear, bearing, and cutting tool coatings. The manipulation of mechanical properties, including strength, hardness, ductility, and morphological stability, is predominantly achievable through the strategic design of microstructures at the nanoscale [12]. A significant body of experimental and theoretical research has investigated these materials' physical and mechanical characteristics. These inquiries encompass an array of properties, such as hardness [13–15], plasticity, fracture behavior [16–17], fatigue properties [18–20], and internal stress dynamics [21–23].

Numerous MNFs have mechanical flaws that impair their functionality. To increase MNFs' dependability, looking into their mechanical properties and processing is crucial. However, detecting the mechanical characteristics and processing reactions of MNFs presents considerable obstacles for experimental approaches, especially in the case of atomic-scale sliding friction. Molecular dynamics (MD) simulations are useful for studying metallic nanolaminates' deformation behavior. These methods are widely used to investigate the mechanical properties of multilayer structures [24] and are increasingly used to examine the development of atomic-level flaws. This comprises nano-indentation

* Corresponding author.
E-mail address: fang@nkust.edu.tw (T.-H. Fang).

https://doi.org/10.1016/j.jnoncrysol.2025.123682
Received 22 March 2025; Received in revised form 9 May 2025; Accepted 18 June 2025
Available online 23 June 2025

[25,43], nano-scratching [26–28], tension [29–33], nano-cutting [34, 35], and cyclic plasticity [36–42].

Cu/Zr MNFs are categorized as quasi-brittle materials, and at room temperature, they usually exhibit little tension ductility. The mechanical properties and deformation behaviors of Cu/Zr MNFs have been the subject of numerous experimental investigations [44–50], while other studies [51–56] have used molecular dynamics (MD) simulations to examine these properties. It is difficult to ascertain experimentally how temperature, growth direction, and layer count affect the mechanical properties of Cu/Zr MNFs.

The mechanical behavior of Cu/Zr MNFs is investigated in this study using molecular dynamics (MD) simulations with the assistance of machine learning to examine the effects of temperature, strain rate, and layer design. Microstructural evolution and stress-strain responses are investigated. The paper is organized as follows: The MD modeling techniques are described in Section 2; the tension and compression loading processes of Cu/Zr MNFs are explained in Section 3; the main deformation mechanisms are examined in Section 4; and the study's conclusions are summarized in Section 5.

Machine learning (ML) is a powerful tool for analyzing large datasets by training models that can perform classification, feature selection, and outcome prediction in new experiments. It also supports researchers in data-intensive fields by helping design experiments to optimize performance or improve hypothesis testing efficiency. ML transforms data collection, analysis, and interpretation across various scientific domains, including nano-optoelectronics, catalysis, and bio-nano interfaces. These approaches are expected to develop into domain-specific standards, further integrating statistical methods into research. Additionally, the field of nanoscience offers the potential to propel ML forward by developing electronic or photonic hardware designed for more efficient algorithm implementation compared to traditional computing systems. Enhancing collaboration between these fields would benefit both scientific communities significantly.

This study will use ML techniques to predict stress values from molecular dynamics (MD) simulation data. The growing application of ML in materials science has been driven by its numerous benefits. For example, real-world experiments with superconducting materials are often expensive and complex to carry out [57]. Deep learning has emerged as a highly effective and reliable approach for applications in materials science [58]. Specifically, integrating ML with MD simulations has improved the accuracy of predicting mechanical properties of high-entropy alloys (HEAs), showing consistent results across both techniques. This integration bridges the gap between MD and ML, significantly reducing the time, cost, and effort involved in experimental testing while also accelerating advances in nanomaterial research and applications, as demonstrated by [59].

This study aims to compare different machine learning techniques applied to predicting stress values from molecular dynamics (MD) simulation data. These include traditional generative models like Gaussian Process Regression and more modern neural network-based approaches, such as feedforward neural networks, convolutional neural networks, recurrent neural networks, long short-time memory, and gated recurrent networks.

2. Methodologies analysis and research hypotheses

2.1. Model of MD simulation

The samples were subjected to uniaxial tension and compression loads, as shown in Fig. 1, and the results were analyzed to determine the plastic deformation properties of Cu/Zr MNFs. Fig. 1 shows the various structural arrangements. The copper-oriented face-centered cubic (FCC) arrangement is shown in red, the zirconium-oriented hexagonal close-packed (HCP) arrangement is shown in blue, the body-centered cubic (BCC) arrangement is shown in blue, and the amorphous configuration is shown in gray. Before reaching thermal equilibrium, the sample had a recognizable arrangement of atomic layers. Both face-centered cubic (FCC) and hexagonal close-packed (HCP) metallic multilayer films displayed a preference for alignment along the [1 1 1] plane, thereby necessitating the adoption of this orientation across all numerical simulation investigations. The physical model of the simulation is the Cu/Zr ingot shown in Fig. 1. The model size is 400×150×50 $Å^3$ (LxWxH), consisting of 188,446 atoms. The model comprises 50 % Cu and 50 % Zr layers arranged horizontally. The specimens consist of alternating Cu and Zr layers with thicknesses of 2.5, 3.33, 4, 5, 6.67, and 10 nm, corresponding to 16, 12, 10, 8, 6, and 4 total layers, respectively. The conjugate gradient method is employed to attain specimens exhibiting minimal potential energy, facilitating the establishment of workpieces in a stable configuration before subjecting them to compressive and tensile loading procedures [60,61]. The simulation involves four main stages: initial relaxation, heating, holding, and quenching. A crystalline CuZr alloy is first relaxed at 300 K for 50 ps. It is then gradually heated to 2500 K over 44 ps, followed by a 40 ps holding period to ensure complete phase transformation to the liquid state. The system is subsequently quenched to 300 K over 25 ps to obtain an amorphous glassy structure [62,63]. Periodic boundary conditions (PBCs) are applied in all three spatial directions. The simulations are conducted in the isothermal-isobaric (NPT) ensemble, with the pressure maintained at zero. A time step of 2 fs is used throughout the simulation. The loading scenarios involve tension and compression along the x-axis, maintained at constant strain rates ranging from 10^{10} to 10^{8} s^{-1}. Deformation loading is regulated by strain amplitude ($\varepsilon = \pm 0.1$).

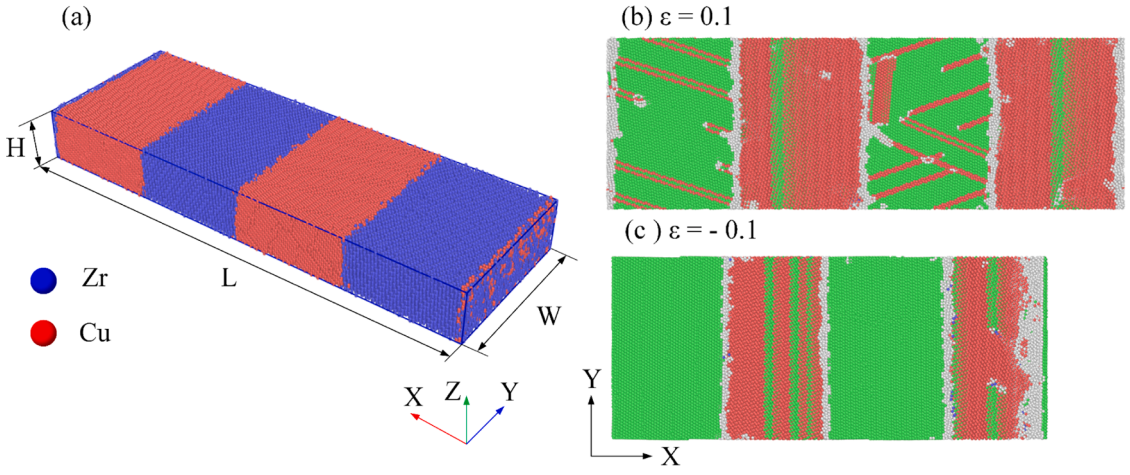

Fig. 1. The diagram of the atomistic model of Cu/Zr MNFs structures during the modeling simulation process(a), tension (b), and compression process (c).

Ensuring thermodynamic equilibrium requires a relaxation period of 200 picoseconds, conducted at 200 K to 600 K.

Molecular dynamics (MD) simulations were performed using the open-source software LAMMPS [64]. Interatomic interactions among Cu–Cu, Zr–Zr, and Cu–Zr pairs were described using the many-body embedded atom method (EAM) potential [65], with parameterizations developed by Mendelev et al. [66,67], for modeling atomic interactions in the workpiece. Post-processing and visualization of simulation outcomes are executed through the open-source visualization tool OVITO [68,69]. Atomic structural distinctions are identified via the joint neighbor analysis (CNA) method [70], while the dislocation extraction algorithm (DXA) [71,72] is employed to scrutinize dislocation structures. All simulations are performed under standard constant temperature (NVT) ensemble conditions, with temperature regulation accomplished using the Nose-Hoover thermostat technique.

2.2. AI algorithms prediction

2.2.1. The gaussian process regression and kernel methods

Gaussian Process Regression (GPR) is a powerful, non-parametric Bayesian approach for regression tasks [73]. Unlike linear or polynomial models, which assume a specific form for the data, GPR uses a probabilistic framework to estimate the distribution over possible functions that fit the data. This allows for high flexibility, especially when working with complex, noisy data, e.g., from material engineering [74].

a. Overview of GPR

GPR defines a prior over functions $f(x)$ that model the relationship between inputs and outputs, with the assumption that these functions follow a multivariate Gaussian distribution [73]. The central idea is that any finite set of function evaluations $f(x_1), f(x_2), \ldots, f(x_n)$ follows a joint Gaussian distribution. The key elements in this process are the mean function and the covariance function (also known as the kernel). The mathematical model for GPR is:

$$y(x) = f(x) + \epsilon \tag{1}$$

where $y(x)$ represents the observed output, $f(x)$ is the true function we aim to learn, and $\epsilon \sim N(0, \sigma^2)$ is Gaussian noise.

The Gaussian Process prior to $f(x)$ is defined as:

$$f(x) \sim GP(m(x), k(x, x')) \tag{2}$$

where, $m(x)$ is the mean function, typically set to 0 unless prior knowledge suggests otherwise, and $k(x, x')$ is the covariance function (or kernel) that measures the similarity between data points.

b. Predictive Distribution

Given a training set $\{(x_i, y_i)\}_{i=1}^{n}$, the GPR model provides a posterior distribution for predictions at new input points x_*. This posterior is Gaussian, with mean and variance given by:

$$\mu_* = K(X_*, X)K(X, X)^{-1}y \tag{3}$$

$$\Sigma_* = K(X_*, X_*) - K(X_*, X)K(X, X)^{-1}K(X, X_*) \tag{4}$$

Where, $K(X, X)$ is the covariance matrix between training points, $K(X_*, X)$ is the covariance matrix between the test and training points, μ_* is the mean prediction for the new input, and the Σ_* represents the uncertainty.

2.2.2. Kernel functions in GPR

The choice of kernel (covariance function) is critical to the performance of the GPR model [75]. The kernel determines how the model measures similarity between input data points and thus governs the shape of the functions that can be fitted. Below are some of the most widely used kernel functions.

a. Squared Exponential Kernel (RBF Kernel)

The Squared Exponential (SE) kernel, also known as the Radial Basis Function (RBF) kernel, is given by:

$$k(x, x') = \sigma_f^2 \exp\left(-\frac{(x - x')^2}{2l^2}\right) \tag{5}$$

Where, σ_f^2 is the signal variance, controlling the amplitude of variation, and l is the length scale, determining how quickly the function varies.

b. Matern Kernel

The Matern kernel family is more flexible than the SE kernel in controlling smoothness. It is given by:

$$k(x, x') = \frac{2^{1-\nu}}{T(\nu)}\left(\frac{\sqrt{2\nu}\| x - x' \|}{l}\right)^{\nu} K_\nu\left(\frac{\sqrt{2\nu}\| x - x' \|}{l}\right) \tag{6}$$

where K_ν is the modified Bessel function of the second kind. Common choices are $\nu = 3/2$ and $\nu = 5/2$, producing once and twice differentiable functions, respectively.

c. Rational Quadratic Kernel

The Rational Quadratic (RQ) kernel generalizes the SE kernel, and is defined as:

$$k(x, x') = \sigma_f^2\left(1 + \frac{(x - x')^2}{2\alpha l^2}\right)^{-\alpha} \tag{7}$$

where α controls the relative weighting of different length scales.

d. Linear Kernel

The Linear kernel models linear relationships between inputs and outputs, and is given by:

$$k(x, x') = \sigma_b^2 + \sigma_v^2\langle x, x'\rangle \tag{8}$$

where σ_b^2 is a biased term, and σ_v^2 controls the linear scaling.

2.2.3. Discriminative ML predictive models

In addition to GPR, deep learning techniques offer powerful alternatives for regression tasks. This section explores the effectiveness of neural network-based methods for predicting stress values from MD simulation data, effectively used in a recent study [59]. These models will be compared regarding evaluation metrics, complexity, and computational resources.

1. Feedforward Neural Network (FFNN): A basic neural network model with multiple layers. For each layer, the output is computed as:

$$y = f(Wx + b) \tag{9}$$

where W and b are the weights and biases, and f is the activation function.

2. Convolutional Neural Network (CNN): Primarily used for image data, CNNs can also capture local dependencies in sequential data using convolutional layers:

$$y = W_f \cdot (\mathrm{ReLU}(W_c * x + b_c)) + b_f \tag{10}$$

3. Long Short-Term Memory (LSTM): LSTM networks capture long-term dependencies in sequences by maintaining a memory state:

$$h_t = o_t \odot \tanh(c_t) \tag{11}$$

where o_t is the output gate, and c_t is the cell state.

4. Bidirectional LSTM (BiLSTM): An extension of LSTM that processes input sequences in both forward and backward directions:

$$h_t = \left[\overrightarrow{h_t}, \overleftarrow{h_t}\right] \tag{12}$$

5. Gated Recurrent Unit (GRU): A simplified variant of LSTM that combines the forget and input gates:

$$h_t = (1 - z_t) \odot h_{t-1} + z_t \odot \widetilde{h_t} \tag{13}$$

6. Recurrent Neural Network (RNN): RNNs model sequences by maintaining a hidden state that evolves:

$$h_t = \tanh(W_h \cdot [h_{t-1}, x_t] + b_h) \tag{14}$$

By comparing these models, we aim to identify the most effective method for predicting stress values from MD simulations, balancing model complexity, accuracy, and computational efficiency.

2.2.4. Evaluation metrics

When developing a regression model, it is essential to assess its performance using a variety of evaluation metrics. These metrics provide insight into the model's learning and predictive accuracy. Below are descriptions and mathematical expressions for key metrics:

Mean Absolute Error (MAE): MAE measures the average magnitude of errors between paired observations, reflecting the same phenomenon. It is calculated by taking the mean of the absolute differences between predicted values and actual values:

$$MEA = \frac{1}{n}\sum_{i=1}^{n}\left|y_i - y_{pred,i}\right| \tag{15}$$

Root Mean Squared Error (RMSE): RMSE is a quadratic scoring rule that represents the average magnitude of the error. It is the square root of the mean of the squared differences between predicted and actual values:

$$RMSE = \sqrt{\frac{1}{n}\sum_{i=1}^{n}\left(y_i - y_{pred,i}\right)^2} \tag{16}$$

R-squared (R^2): Also known as the coefficient of determination, R^2 indicates how well the data fit the regression model. It represents the proportion of the variance in the dependent variable that is predictable from the independent variables:

$$R^2 = 1 - \frac{\sum_{i=1}^{n}\left(y_i - y_{pred,i}\right)^2}{\sum_{i=1}^{n}(y_i - \bar{y})^2} \tag{17}$$

Where, y_i represents the actual value, $y_{pred,i}$ denotes the predicted value, $\bar{y}$ is the mean of the actual values, and n is the total number of observations.

3. Analysis of the results and discussion

3.1. Results of MD simulation

3.1.1. Impact of temperature

This segment involves subjecting the workpiece to uniaxial tension and compression under thermal conditions of 200, 300, 400, 500, and 600 K with strain rates of 10^9 s^{-1} and 4 layers of Cu/Zr.

Fig. 2 depicts stress-strain curves acquired from the experimental data, presenting absolute stress and strain measurements for comparative analysis. The stress levels exhibit a linear progression until reaching their peak magnitudes across all curves, followed by a sudden decline, indicative of transitions between elasticity and plasticity. This phenomenon is attributed to the expansion of dislocations and significant sliding within flawless crystalline structures. Within molecular dynamics (MD) simulations, the stress point corresponding to this decline is commonly called yield stress, as established by previous studies [76]. The MNFs have more valuable yield stress under tensile loading than compressive loading. Elevated temperatures induce atomic expansion, with varying materials exhibiting distinct coefficients of thermal expansion, thereby generating thermal prestressing forces within the film. This phenomenon is elucidated by findings indicating a direct correlation between temperature elevation and heightened atomic activity, resulting in material softening and a subsequent decrease in yield strength. Specifically, under tensile loading conditions, the yield strengths are 4.727, 4.011, 3.501, and 3.500 GPa at temperatures 300, 400, 500, and 600 K, respectively. Conversely, during compression, the corresponding yield strengths are measured at 2.828, 2.443, 2.294, and 2.138 GPa for the exact temperature increments.

Under equivalent circumstances, there is a notable discrepancy in the compressive curves compared to the tensile curves. Besides, the fluctuation of stress-strain curves in the tensile process under the influence of temperature is more stable than in the facilitation of the compression process due to elevated resistance against dislocation slip, particularly notable at lower temperatures. In theory, the lattice abrasion $\tau_f$can be estimated [77,78]:

$$\tau_f = \frac{2G}{1-v}\exp\left[\frac{-2\pi w}{b}\right] \tag{18}$$

This scenario illustrates the phenomenon of lattice friction shear, the characteristics of dislocation core breadth, and the Burgers vector b. It also involves the representation of Poisson's ratio v, and shear modulus G, alongside the normalization of the width of the dislocation center by the Burgers' vector w/b [79,80]:

$$\frac{w}{b} = \left(\frac{w}{b}\right)_0 \exp\left(\frac{T}{3T_m}\right) \tag{19}$$

Where T_m represents the melting point, its value is $(w/b)_0$ at absolute zero temperature. As temperature decreases, the width of the dislocation core diminishes, thereby augmenting lattice friction. The initiation of dislocation slip at 200 K exhibits more incredible intricacy than that at 300 K, 400 K, 500 K, and 600 K, resulting in more uniform deformation at the former temperature. Moreover, as depicted in Fig. 3, the common neighbor analysis (CAN) technique is employed to scrutinize the progression of dislocations during tensile and compressive procedures across various temperature settings and strain rate parameters. The depiction of lattice structures within the material is delineated in the red and green segments, representing the hexagonal close-packed (HCP) and face-centered cubic (FCC) arrangements, respectively, whereas areas in white denote lattice irregularities. Within molecular dynamics (MD) simulations, a twin boundary (TB) signifies a layer of HCP slab encompassing at minimum two HCP layers, an intrinsic stacking fault (ISF) pertains to two contiguous HCP layers, and an extrinsic stacking fault (ESF) refers to two HCP layers adjacent to a solitary internal FCC layer [81].

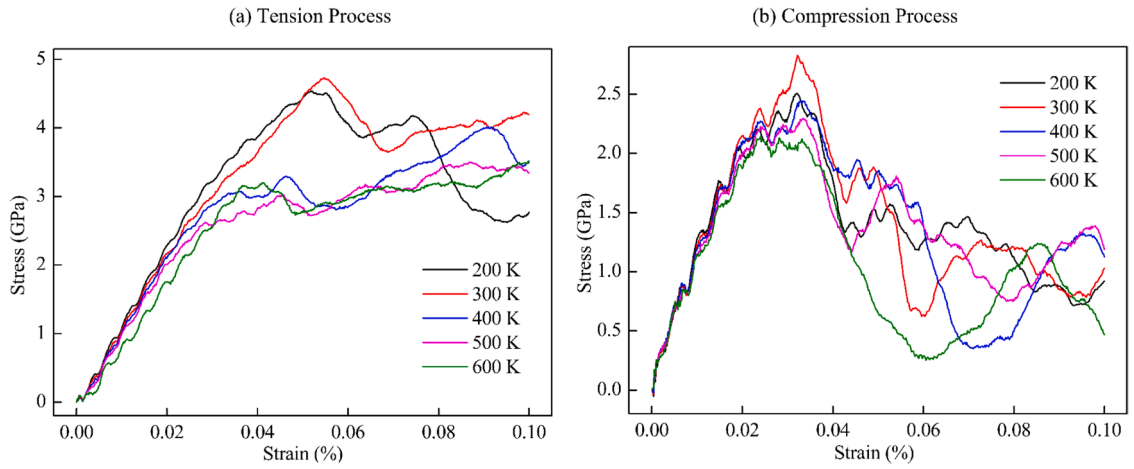

Fig. 2. Stress-strain curves with different temperatures under uniaxial tension and compression.

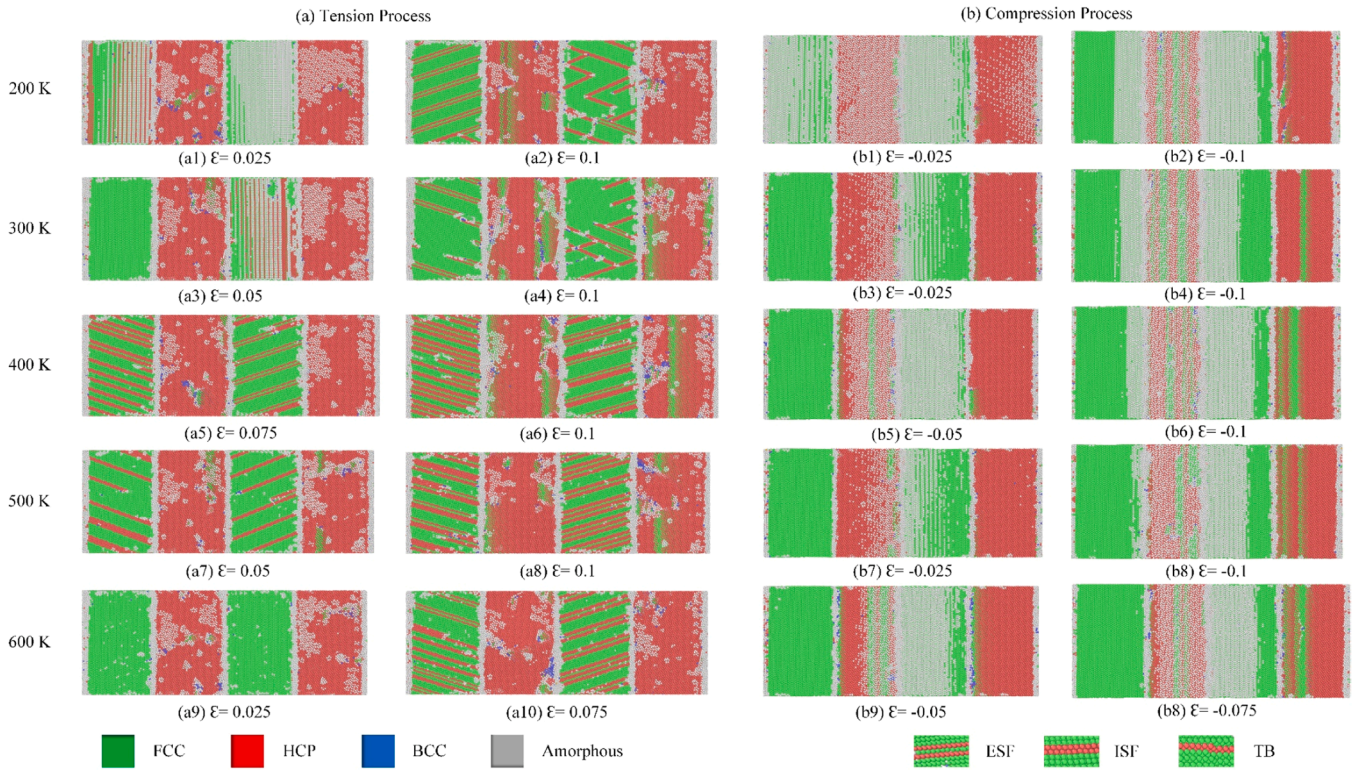

Fig. 3. The common neighbor analysis (CAN) under tension and compression process with stain rate of 10^9 s^{-1} and various temperatures.

The tension-compression asymmetry is akin to the pressure-induced dislocation mobility, as evidenced in molecular dynamics simulations of nanocrystalline copper and copper nanocubes [82,83], and is noteworthy. It is observed that under decreasing stress conditions, the stable compressive stresses are comparatively lower than tensile stresses at equivalent temperature and strain rates. Moreover, the deformation behavior of MNFs is notably influenced by variations in temperature and strain rates [84]. The experimental observations of Cu/Zr MNFs [84] are equivalent to this phenomenon. When dealing with materials exhibiting tensile strength, a notable augmentation in yield stress poses a more conspicuous and challenging issue. Moreover, it is noteworthy that temperature influences the monotonic deformation of Cu/Zr MNFs; nonetheless, this impact is relatively minor compared to the strain rate effect. Under conditions characterized by compressive circumstances at a temperature of 300 K, alongside a strain rate of 10^{10} s^{-1}. The more significant the change in tensile speed, the more pronounced the effect on yield stress.

The dynamic response of the workpieces to various temperatures under the tension and compression process with strain rates of 10^9 s^{-1} values is shown in Fig. 3. The first observation indicates that the phase transformation and structural destruction are aggravated for both specimens with increasing temperature values. The phase transformation in all samples with different temperatures is similar. The FCC phase transforms to the HCP phase with stacking faults in the Cu layers, and the structural change from HCP to the amorphous structure is dominant in the Zr layer. Besides, it is the appearance of a small part of the BCC phase. The mechanical response of Cu/Zr MNFs has apparent differences in various temperatures in all cases. At low temperatures of 200 K and 300 K, many stacking faults occur in the Cu layers, and the amorphous structure has appeared in the Zr layers. Meanwhile, these

stacking faults are strongly decreased, and the amorphous structure increases sharply at higher temperatures, such as 500 K and 600 K.

The dislocation evolution of Cu/Zr MNFs samples with various temperatures during the tension and compression process under various strain rates is shown in Fig. 4. The dislocation growth originates at the interface between the Cu and Zr layers. Shockley partial dislocation dominates the deformation evolution in the Cu and Zr layers, while Frank partial dislocation occurs in both Cu and Zr layers. In addition, the substantial increase in the dislocation network is proportional to the temperature increase.

Fig. 5 depicts the variation in workpiece dislocation density under tension and compression at different temperatures. Notably, the dislocation density is markedly higher in workpieces subjected to lower temperatures than those at higher temperatures. Overall, there is a consistent decrease in dislocation density with rising temperature across all scenarios. Substantial dislocation density augments are observed at lower temperatures, notably 200 K and 300 K, under tension and compression. Specifically, the tensile process exhibits a pronounced increase in dislocation density at 200 K. Conversely, at higher temperatures, such as 500 K and 600 K, a marginal escalation in dislocation density is noted for both tension and compression processes.

Fig. 6 Observations reveal the reduction, flexion, and branching of shear bands (SBs) within the amorphous layers surrounding local operating workpieces. For instance, SBs denoted as "Sb B" and "Sb D" halt their transmission through the decomposition of their shear fronts into multiple dislocations, thereby inducing intersecting dislocation slips within the nanograins. Additionally, SBs labeled "Sb A" and "Sb C" deviate from their original shear planes by branching near the Cu layers. At the same time, those marked as "Sb A" tend to divert deformation along the grain boundaries (GBs) upon encountering them. Notably, most nascent SBs are arrested by the Cu layers, with only a minority penetrating the Cu nanograins directly. The interactions between propagating SBs and Cu layers act to suppress the formation of mature SBs and delay the onset of shear instability. Consequently, increased activation of secondary SBs and dislocations near the constrained amorphous interfaces (CAIs) are observed to accommodate the local plastic deformation induced by obstructed SBs. Intensive deformation fosters the synergistic engagement of shear bands (SBs) and dislocations within the interface of amorphous and copper layers, as evidenced by the interweaving patterns of shear and slip bands occurring at a strain level of $\varepsilon = \pm 0.1$. Cooperative deformation facilitates the redistribution of plasticity between the two phases, leading to a more homogeneous deformation process and enhanced energy dissipation. Furthermore, this unique cooperative deformation mechanism is a reinforcement mechanism inherent in nanolaminates that alleviates the strain-induced softening stemming from shear localization within the glassy layers [85]. This phenomenon ultimately leads to an elevation in flow stress, as depicted in Fig. 2.

The von Mises stress distribution among atoms within the Cu/Zr sample across varying temperatures is depicted in Fig. 7, wherein atom colors correspond to their respective von Mises stress values. Analysis reveals a predominant high von Mises stress concentration within the grain boundary (GB) region, characterized by elevated shear stress across all samples. This phenomenon can be attributed to the comparatively lower atom density typically observed in GBs, consequently rendering them more susceptible to experiencing heightened stress levels. Furthermore, it is noted that the magnitude of shear stress varies among samples subjected to different temperatures, with stress concentration expanding with increasing temperature owing to the amorphous nature of the structure. Moreover, the findings indicate a proportional increase in the proportion of atoms experiencing elevated von Mises stress levels with rising temperature. Consequently, it is inferred that elevated temperatures exacerbate grain instability, resulting in escalated von Mises stress within the Cu/Zr MNFs sample.

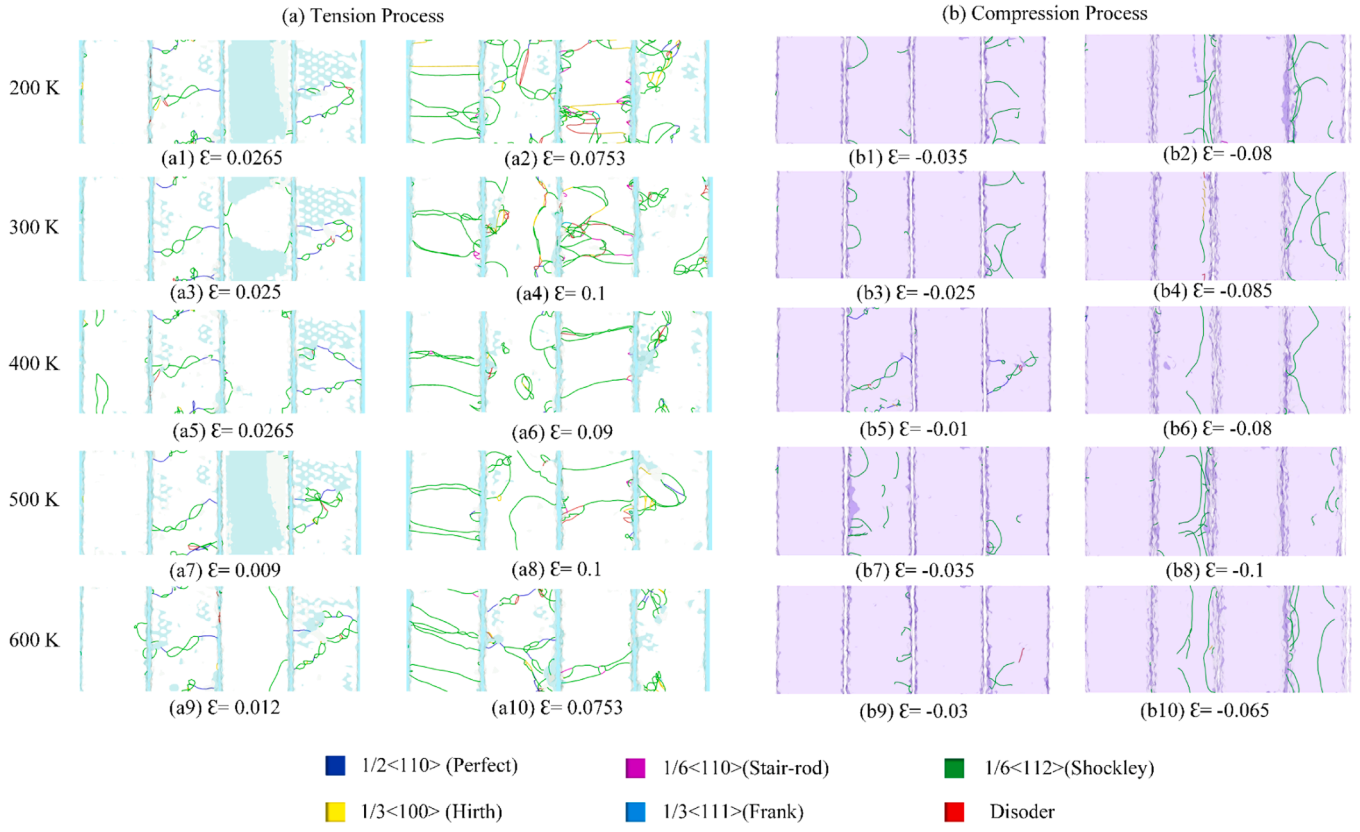

Fig. 4. Snapshots showing the dislocation extraction algorithm (DXA) for the emergence of disorder of Cu/Zr MNFs with various temperatures and strain rates of 10^9 s^{-1}.

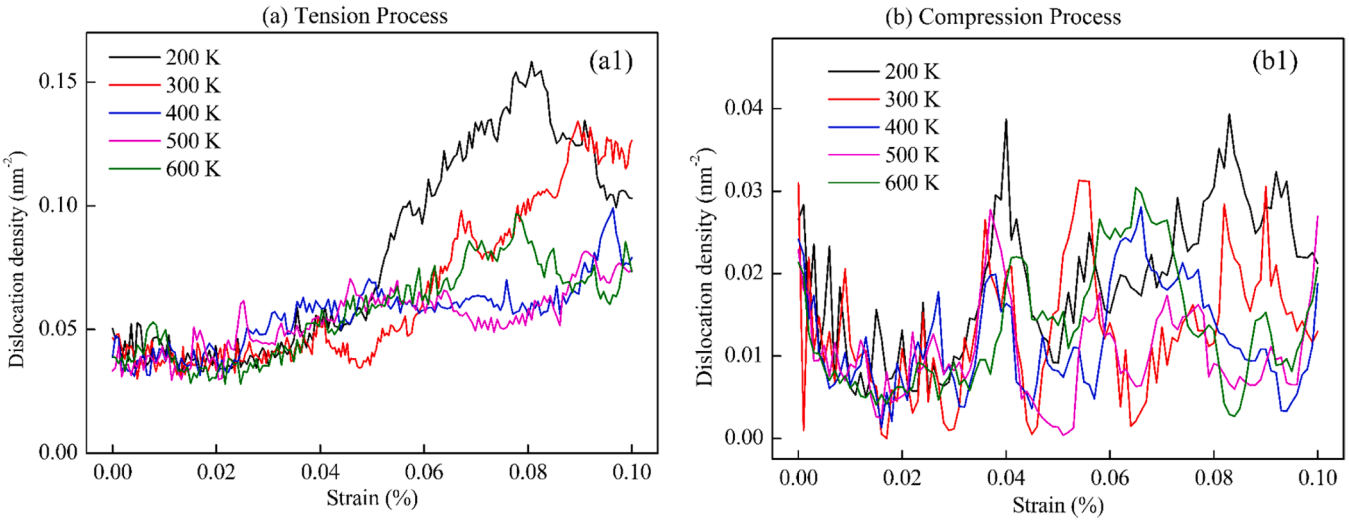

Fig. 5. Evolutions of dislocation densities during the tensile and compressive processes with different temperatures and strain rates of 10^9 s^{-1}.

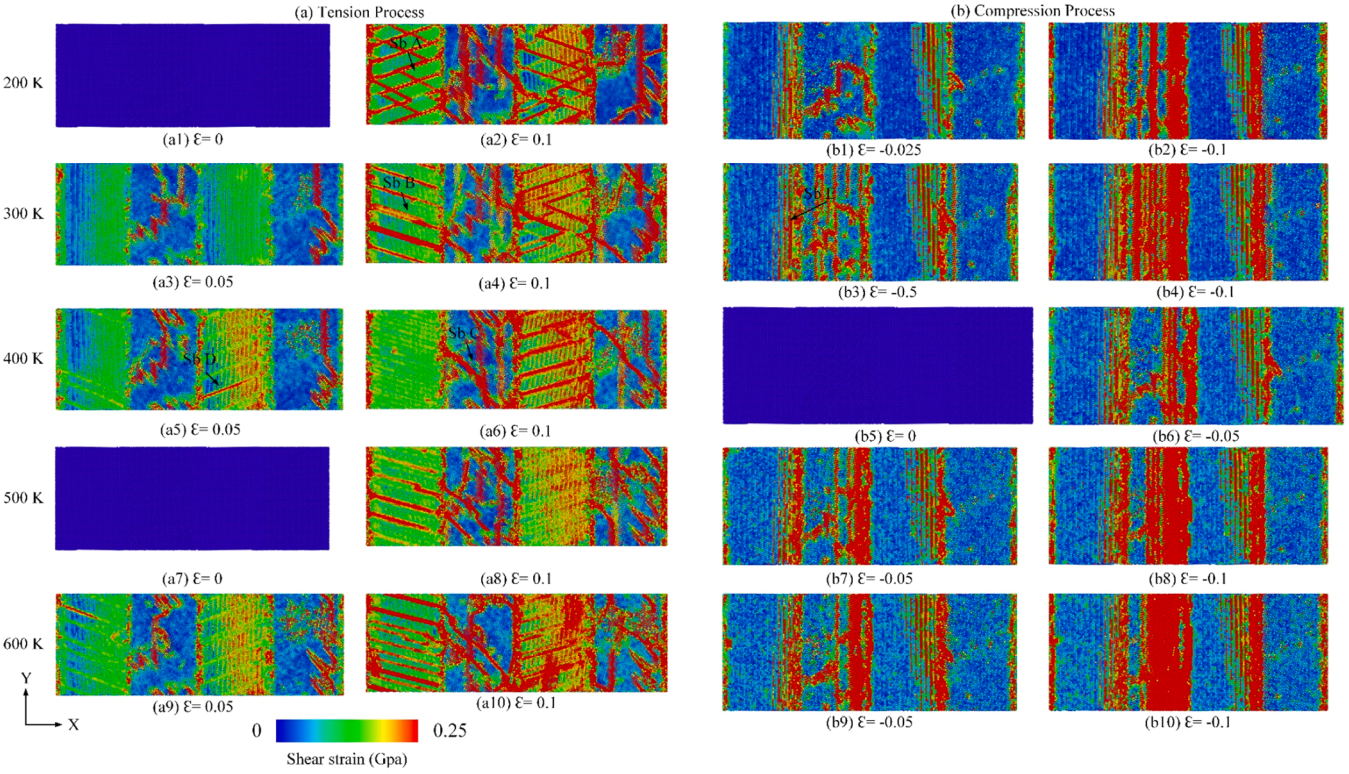

Fig. 6. Shear strain distribution under the tension and compression process at different temperatures, at a strain value of $\varepsilon = \pm 0.1$ and a strain rate of 10^9 s^{-1} and four layers.

3.1.2. *Impact of strain rate*

Five distinct strain rate values are examined to assess the impact of strain rate on the mechanical properties of the Cu/Zr MNFs: 10^8, 5×10^8, 10^9, 5×10^9, and 10^{10} s^{-1}. Specifically, a workpiece comprising four layers and operating at a temperature of 300 K is chosen to scrutinize strain rate effects.

Fig. 8 illustrates the stress-strain behavior of Cu/Zr (MNFs) subjected to varying strain rates under both tensile and compressive loading conditions at a temperature of 300 K. Under tension, the yield strength exhibits an incremental rise from 3.895 to 5.966 GPa as the strain rate escalates from 10^8 to 10^{10} s^{-1}. This augmentation in strain rate reduces the time frame for atomic structural rearrangement during tensile deformation, impeding stress relaxation within the material and yielding elevated stress levels. Notably, this outcome resonates with prior findings reported by Hussain et al. [86] and Potirniche et al. [87] regarding Cu/Zr MNFs and monocrystalline Cu films, respectively. Conversely, under compression, the yield strength progressively increases from 1.700 to 3.851 GPa with the elevation of strain rate from 10^8 to 10^{10} s^{-1}. Notably, within the strain rate range of 5×10^9 to 10^{10} s^{-1}, the tension yield strength experiences a more pronounced escalation than the compression counterpart.

The structural evolutions of Cu/Zr specimens under tension loading at different strain levels at room temperature (300 K) are depicted in Fig. 9. The occurrence of phase transformation coincides with the

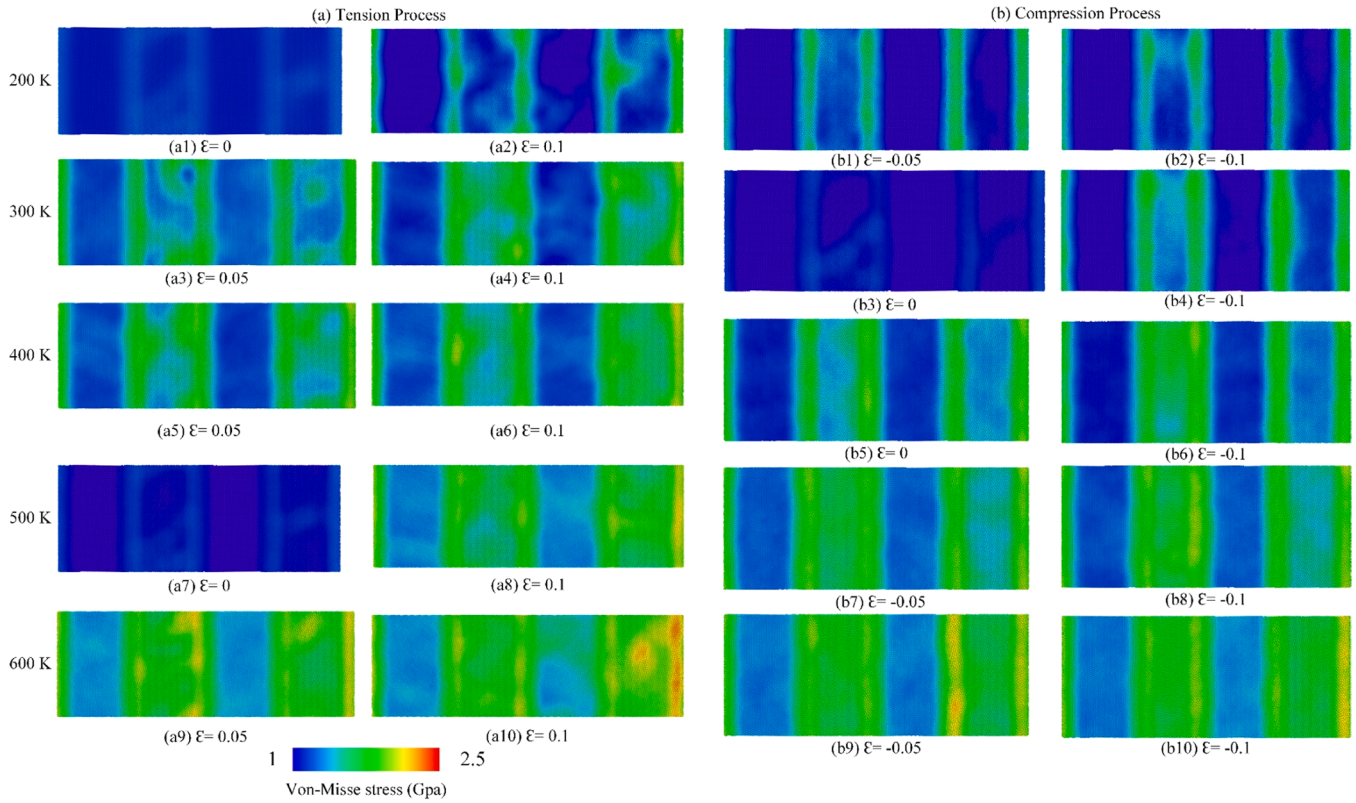

Fig. 7. The von Mises stress distribution of Cu/Zr MNFs with four layers at ± 0.1 strain value strain rate of 10^9 s^{-1} with various temperatures during the tension and compression process.

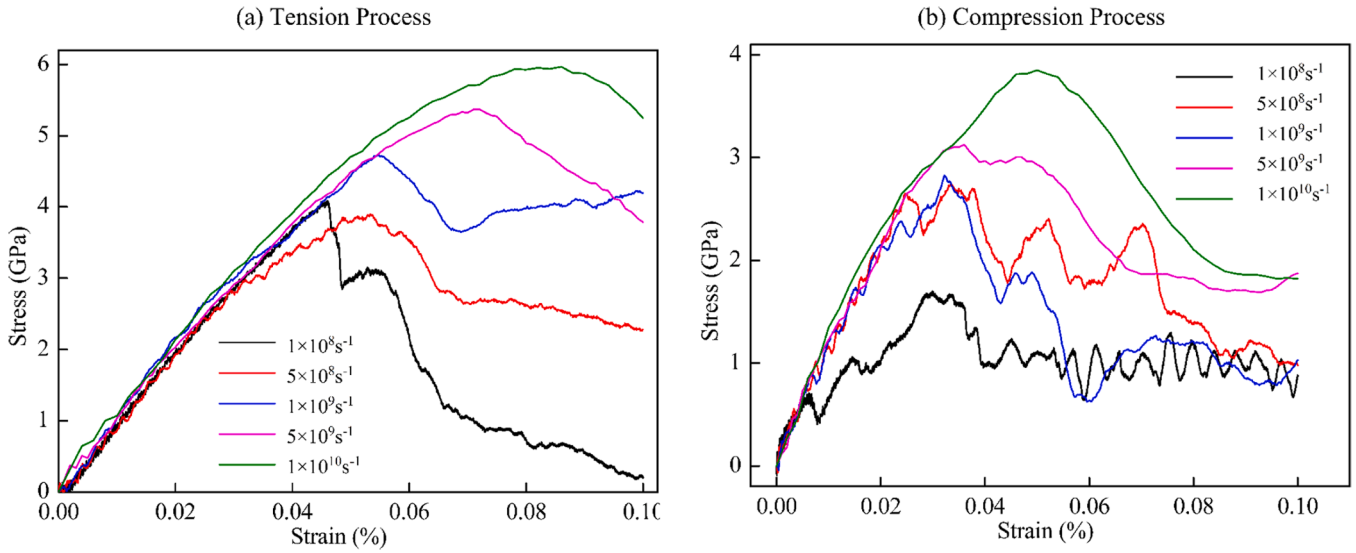

Fig. 8. Stress-strain curves under tension and compression at 300 K with four layers at strain ε = ± 0.1 with different strain rates.

appearance of stacking faults, as illustrated in Fig. 9(a1–a8), wherein stacking faults emerge at the interface of the Cu/Zr multilayer and the Cu layer's intersection during dislocation migration. Our investigation reveals that dislocation motion and phase transformation commence before the onset of yield stress, manifesting at strain levels of 0.025, 0.03, 0.032, 0.05, 0.075, and 0.1, under strain rates of 10^8, 5×10^8, 10^9, 5×10^9, and 10^{10} s^{-1}, respectively. Notably, the presentation of dislocations and phase transformations is delayed with increasing strain rates. The FCC to HCP transition occurs within the Cu layers upon reaching peak stress, concurrent with the transformation of HCP in the Zr layers to amorphous and BCC structures. After peak stress, a substantial generation of oblique stacking faults arises within the Cu layer due to lattice mismatches at the Cu/Zr MNFs interface. This is followed by the continued propagation of stacking faults and dislocations within the Cu layer [88,89], as shown in Fig. 9(a1–a8). Generally, augmenting strain levels enhances the rate of FCC transformation, indicating a robust conversion of Cu layers from FCC to HCP and amorphous structures with increasing strain rates. Conversely, in the Zr layers, elevating strain rates result in a diminished rate of HCP-to-FCC phase transformation, as evidenced in Fig. 9(a1-a8). Furthermore, the phase distribution becomes

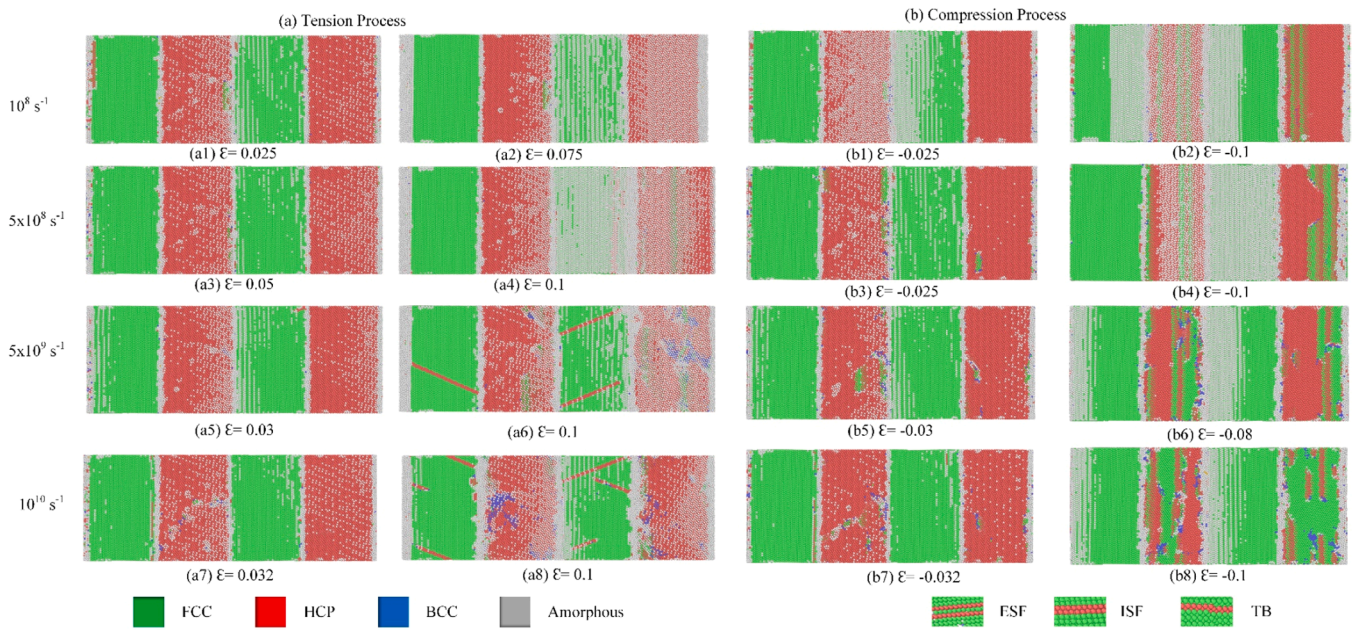

Fig. 9. The common neighbor analysis (CAN) between the tension and compression process at 300 K temperature and various strain rate values.

more homogeneous with increasing strain rates, with less segregation observed in the HCP structure of the Zr layers. This phenomenon is attributed to atoms' shortened rearrangement and relaxation times at higher strain rates, leading to phase transformations within narrower regions.

The structural alterations of Cu/Zr MNFs under compression testing at 300 K are illustrated in Fig. 9(b1-b8), depicting phase transformations coinciding with the onset of dislocation appearance and yield stress, as demonstrated in Fig. 9(b1–b8). During this phase, the phase transition closely mirrors prior observations. Notably, the transition occurring as tension stress surpasses the yield point corresponds to the lowest stress value, as evidenced in Fig. 9(b1-b8). At a high strain magnitude ($\varepsilon = -0.1$), the phase transition of the horizontal sample is delineated in Fig. 9(b1-b8). In contrast to vertical specimens, the compression-induced phase transformation rate exhibits insensitivity to strain rate variations. Additionally, unlike in tension, the HCP structure of Zr layers in compression does not transition to the FCC structure.

Fig. 10 illustrates the distribution of dislocations during tension and compression tests conducted at various strain rates and at a temperature of 300 K. Stair-rod, Shockley partial, and Perfect dislocations emerge nearly at the onset of the tensile process due to lattice mismatches, primarily nucleating at the Cu/Zr layer interface. Shockley dislocations

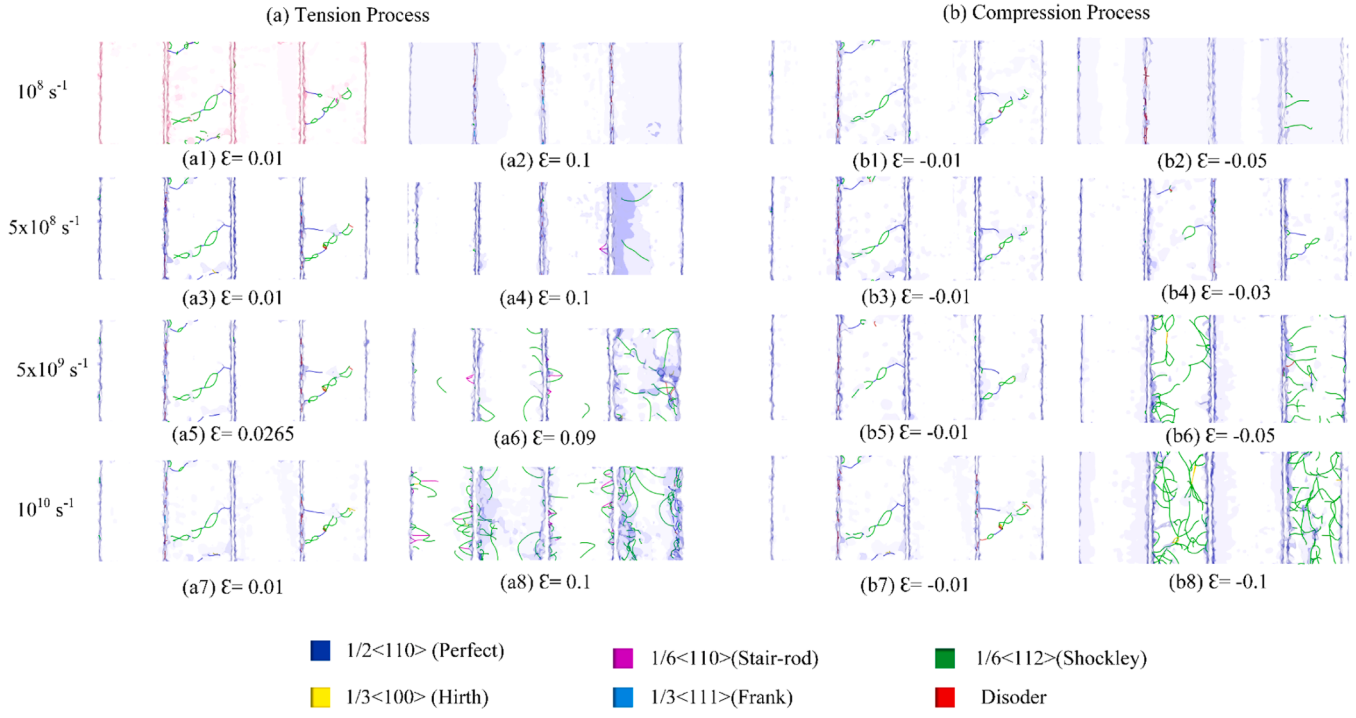

Fig. 10. Snapshots showing the dislocation extraction algorithm (DXA) for the emergence of disorder of Cu/Zr MNFs with various strain rates and temperatures at 300 K.

predominate among the total dislocation population, surpassing other types across all scenarios. The cleavage of Perfect dislocations generates Shockley partial dislocations, while Stair-rod dislocations arise from interactions involving Shockley partials, as depicted in Fig. 10(a1-a10) [47–49]. Moreover, Frank dislocations can engender Shockley partial and Stair-rod dislocations, as evidenced in Fig. 10(b1-b10) [48–50]. However, the presence of Frank dislocations is limited, thereby rendering their influence on mechanical characteristics uncertain.

The deformation evolution of the Cu/Zr MNFs sample across four layers, subject to varying strain values and strain rates, is depicted in Fig. 11. Within Fig. 11(a1-b8), the deformation distribution corresponding to the HCP phase structure transformation of the inclusion is delineated, revealing a near-complete disappearance of the interface between the inclusion and the workpiece. Notably, the strain value at the phase transformation of the inclusion escalates from 0.02 to 0.1 with increasing strain rates from 10^8 s^{-1} to 10^{10} s^{-1}. Fig. 11(b1-b8) portrays a heightened concentration of shear strain encircling the inclusion under elevated strain rates, a phenomenon conducive to greater stress values, as expounded in Fig. 8. Subsequent augmentation in strain values, evidenced in Fig. 11(a3-a4) and (b3-b4), results in the propagation of local deformation within the workpiece via shear bands. Furthermore, at a low strain rate of 10^8 s^{-1}, local strain tends to diffuse throughout the entire workpiece. In contrast, at high strain rates such as 5×10^9 and 10^{10} s^{-1}, local deformation is concentrated in the middle region of the specimen, thereby inducing more pronounced workpiece contraction.

Fig. 12 illustrates the von Mises stress distribution across the atoms within the CuZr sample at various strain rates, with atom colors denoting their respective stress levels. The examination reveals a notable aggregation of von Mises stress within the grain boundary (GB) region, characterized by elevated shear stress across all samples. This phenomenon is attributed to the comparatively lower atom densities inherent to GBs, rendering them more susceptible to heightened stress levels. Furthermore, the amorphous structure contributes to varying magnitudes of shear stress among samples subjected to differing strain rates, with stress concentrations escalating as strain rates increase. Moreover, the findings indicate a direct correlation between increasing strain rate and a heightened fraction of atoms exhibiting elevated von Mises stress levels. Consequently, it is inferred that higher strain rates exacerbate grain instability, leading to an escalation in von Mises stress within the Cu/Zr MNFs sample.

3.1.3. Impact of layer number

The thickness of layers (γ) emerges as a pivotal factor shaping the mechanical attributes of ML materials. This study delves into the impact of layer count on the mechanical characteristics of Cu/Zr MNFs, examining samples comprising 4, 6, 8, 10, 12, and 16 layers at a simulation temperature of 300 K. The uniaxial tension and compression test is conducted at a strain rate of 10^9 s^{-1}. The investigation scrutinizes the impacts of layer number on stress-strain relationships, dislocation behavior, and yield strength in tension and compression layer configurations.

Fig. 13 depicts stress-strain diagrams for Cu/Zr MNFs with varying layer thicknesses and orientations. Both tension and compression diagrams exhibit similar curve patterns, delineated into three regions based on microstructural evolution. In area (I), stress increases linearly during elastic deformation. In Region II, the stress peaks at a strain of approximately 0.04, initiating dislocation nucleation and intense activity within the Cu layers, leading to a rapid stress drop. As shown in Fig. 15, this reflects dislocation-driven energy release. In Region III, the stress stabilizes, and the gap between the yield strength and steady-state flow stress indicates the extent of strain softening. The flow stress stabilizes around 1.5–1.75 GPa in tension and 1.75–2.00 GPa in compression, suggesting that layer thickness has a limited effect on tensile strength, consistent with prior studies.

Fig. 14 illustrates the phenomena of dislocation nucleation and phase transformation occurring under tension and compression loading conditions at 300 K, employing various layer thicknesses and a strain rate of 10^9 s^{-1}. Tensile and compressive forces transition the face-centered cubic (FCC) structure of Cu layers to the hexagonal close-packed (HCP) structure. In contrast, the body-centered cubic (BCC) structure within the zirconium (Zr) layers transforms an amorphous structure. Additionally, the emergence of the HCP structure is attributed to the mechanisms involving stair-rod cross slip, whereby high-stress levels on the intersection of sliding planes lead to the generation of Shockley partial dislocations. Moreover, establishing an HCP region will ensue upon the recurrence of these manipulations across parallel planes interspersed by layers of Cu and Zr. This observation aligns with earlier investigations conducted by Tran [90], Waitz et al. [91], and Yang et al. [92]. This outcome signifies enhanced structural stability in the sample under tensioning conditions [93,94]. Notably, this stability manifests when the yield stress during tension surpasses that of compression, as

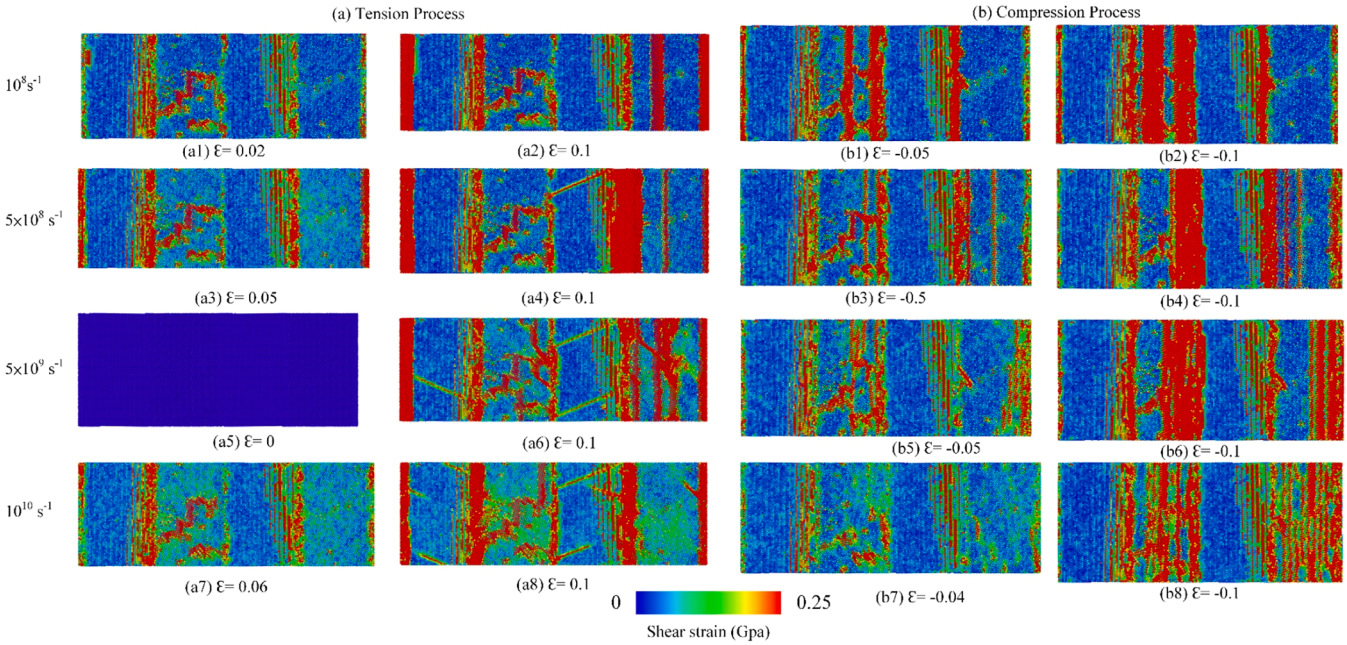

Fig. 11. Shear strain distribution under the tension and compression process at 300 K and four layers with different strain rates.

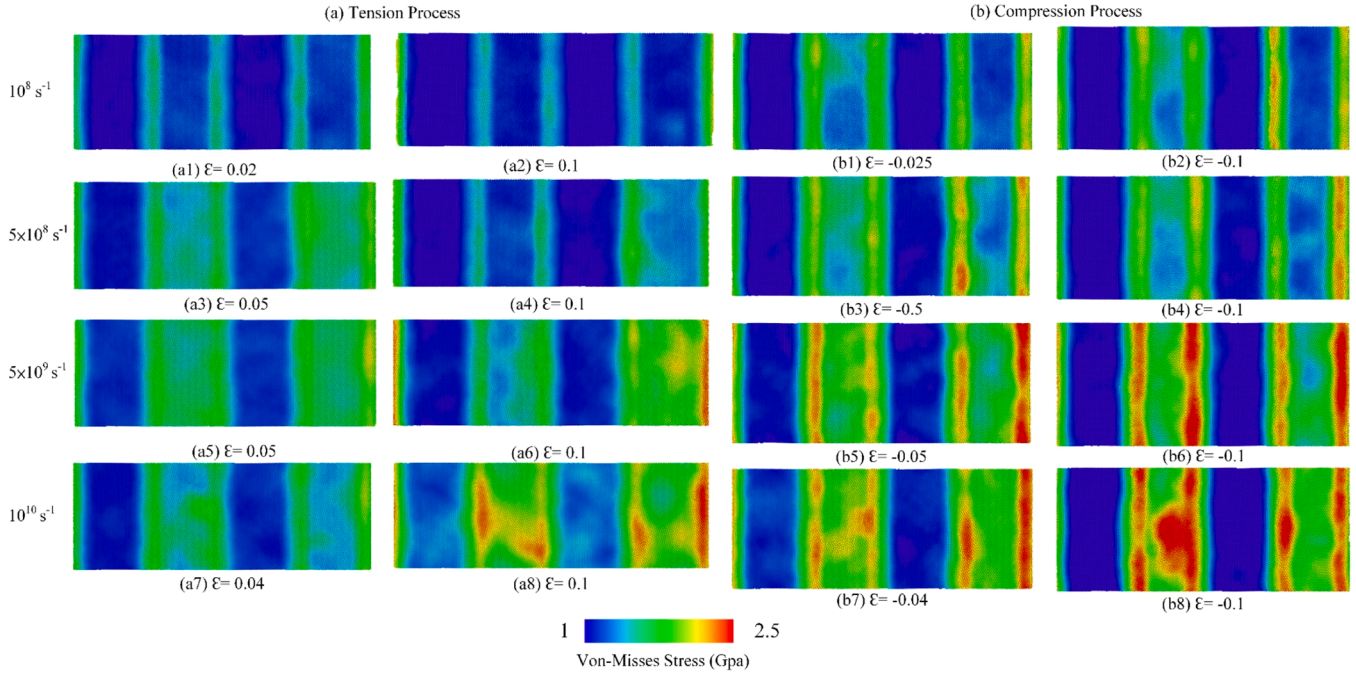

Fig. 12. The von Mises stress distribution of Cu/Zr MNFs at four layers at 300 K with various strain rates under tension and compression.

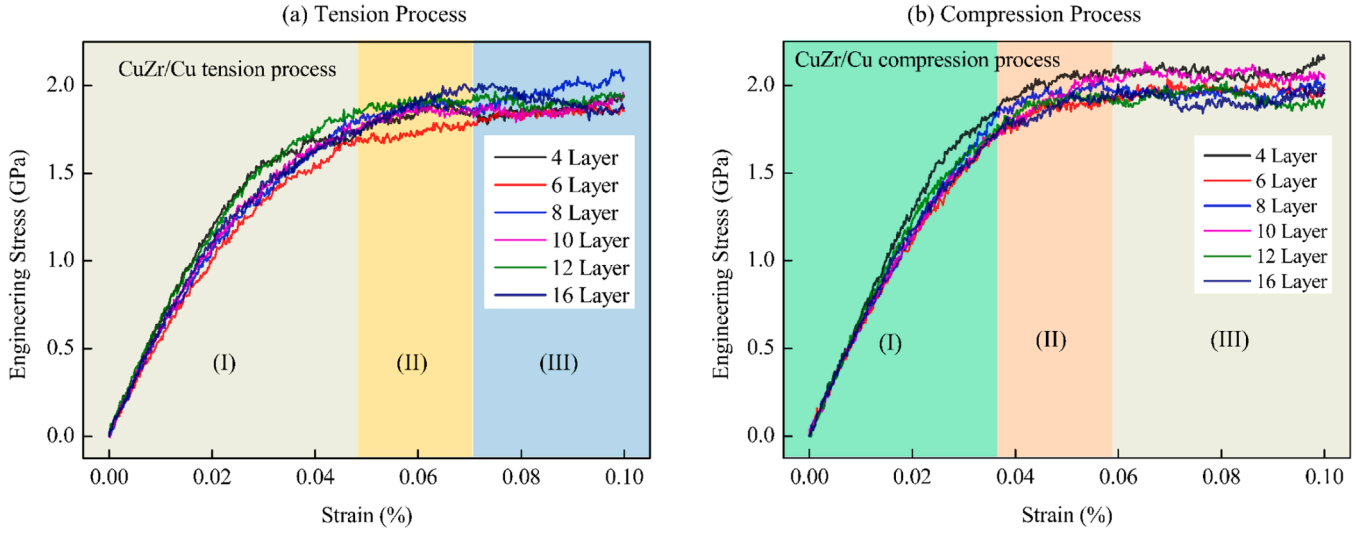

Fig. 13. The stress-strain diagrams of the Cu/Zr MNFs with different layer numbers at 300 K.

depicted in Fig. 13(a-b). Concurrently, the initiation of stacking faults occurs concomitantly with phase transformations within the specimens. As dislocations propagate, twin boundaries and extrinsic stacking faults emerge in the forward progression.

Fig. 15 shows the dislocation distribution during tensile and compressive loading at $\varepsilon = \pm 0.1$, strain rate of 10^9 s^{-1}, and temperature of 300 K across various layer thicknesses. At early stages, Stair-rod, Partial Shockley, and Perfect dislocations emerge due to lattice mismatch, predominantly at Cu/Zr interfaces. Shockley dislocations dominate in all configurations. Cleavage of Perfect dislocations produces Partial Shockley types, observed in 4-layer and 8-layer structures, while interactions among Shockley dislocations generate Stair-rod types. Frank dislocations, though sparse, may also contribute to these mechanisms. As illustrated in Fig. 16, dislocation density increases with decreasing layer thickness due to enhanced interface area, which promotes atoms.

Fig. 16. illustrates the evolution of dislocation density in Cu/Zr samples of varying layer thicknesses under both tension and compression, subjected to a strain rate of 10^9 s^{-1} at 300 K. Dislocation density, defined as the total length of dislocations per unit volume, fluctuates marginally before reaching peak values in the stress-strain diagrams, as evidenced in Fig. 13 and Fig. 14. Subsequently, a slight upward trend in dislocation density is observed during tension and compression processes. Furthermore, reducing the layer thickness generally corresponds to higher dislocation densities in tension and compression. This correlation is attributed to the increased layer area associated with smaller layer thicknesses, facilitating dislocation formation. Conversely, increasing layer thickness restricts dislocation propagation due to interface constraints. Notably, disparities in dislocation density are observed between tension and compression processes. Specifically, tension induces higher dislocation densities compared to compression. This discrepancy arises from the minimal occurrence of phase

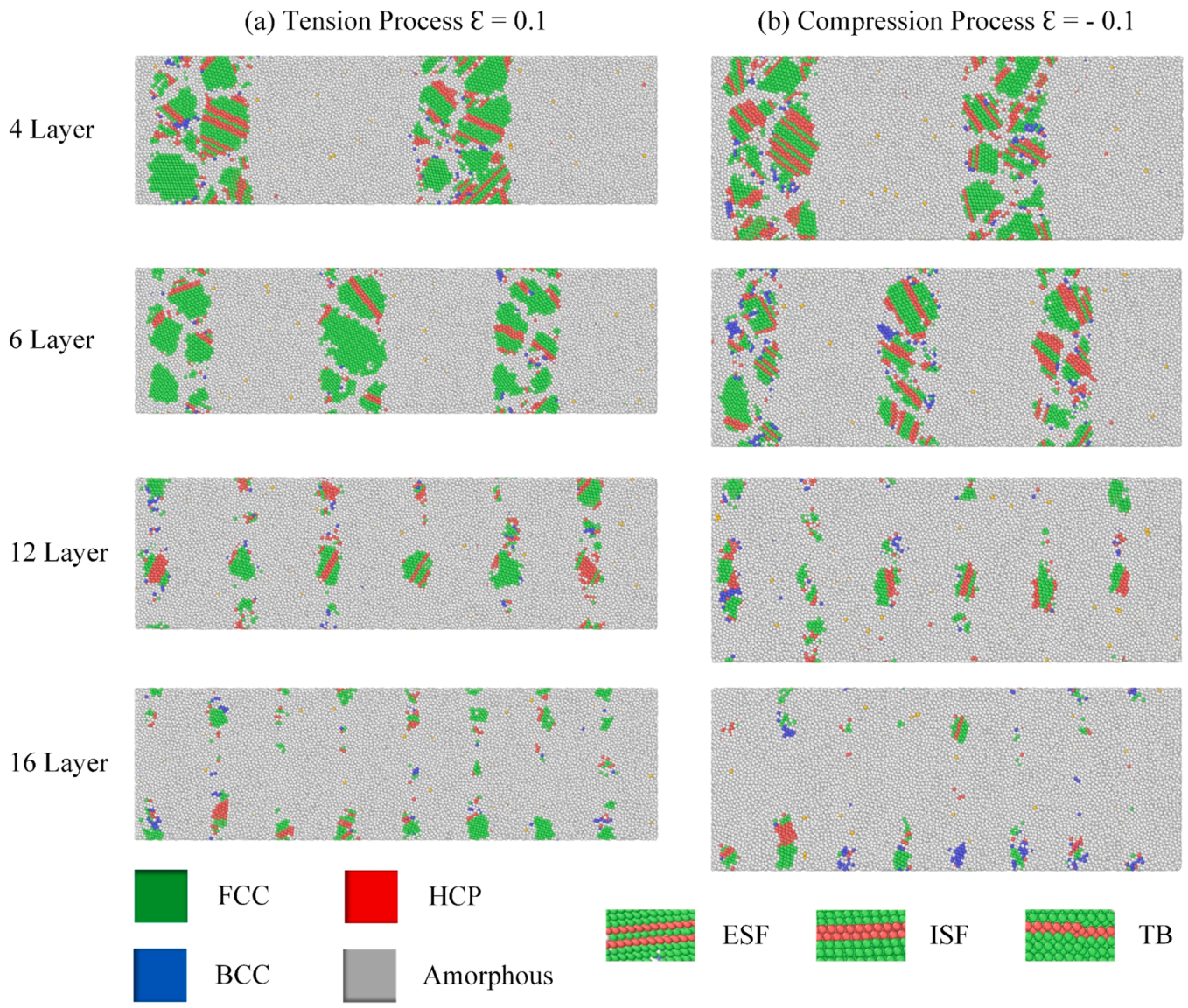

Fig. 14. The CNA monitors the structural evolution in the Cu/Zr MNFs at 300 K and strain rate of 10^9 s^{-1} with different layers.

transitions in the Zr layers during tensile loading, as depicted in Fig. 14, leading to the absence of dislocations in these layers, as illustrated in Fig. 15.

The Cu/Zr MNFs sample's deformation evolution across different layers, subjected to strain rates of 10^9 s^{-1}, is illustrated in Fig. 17. Within the subfigures denoted as (a1-b8), the deformation distribution corresponding to the HCP phase structure transformation of the inclusion is depicted, indicating a substantial reduction in the interface between the inclusion and the workpiece. Remarkably, the strain value at the phase transformation of the inclusion increases from 0.05 to 0.1 with a rise in layers from 6 to 16. Fig. 17 demonstrates an intensified concentration of shear strain surrounding the inclusion under higher layers, leading to heightened stress values, as elucidated in Fig. 13. Subsequent increments in strain values, as observed in Fig. 17, result in the propagation of local deformation within the workpiece through shear bands. Moreover, local strain disperses distinctly at lower layers such as 6 and 8 throughout the workpiece. Conversely, at higher layers, such as 12 and 16 layers, local strain diffusion throughout the entire workpiece is less evident, thereby inducing a less pronounced workpiece contraction.

Fig. 18 Presents the von Mises stress distribution across atoms within the Cu/Zr MNFs at various layers, employing atom colors to signify stress levels. The analysis unveils a pronounced accumulation of von Mises stress within the grain boundary (GB) region, characterized by heightened shear stress across all specimens. This occurrence is ascribed to the relatively lower atom densities inherent in GBs, rendering them more susceptible to elevated stress levels. Additionally, the amorphous structure contributes to divergent magnitudes of shear stress among samples with different layers, with stress concentrations diminishing as layers increase. Furthermore, the results indicate a direct association between increasing layers and a decreased proportion of atoms manifesting lower von Mises stress levels. Consequently, it is deduced that higher layers mitigate grain instability, reducing von Mises stress within the Cu/Zr MNFs sample.

3.2. Results with the assistance of AI prediction

3.2.1. Data

To gather the data necessary for training and predicting stress values, we performed Molecular Dynamics (MD) simulations on a system with the following specifications: i) Processor: Intel(R) Core(TM) i7–10,700 CPU @ 2.90 GHz (16 CPUs) and ii) Memory: 16GB RAM.

Tables 1 and 2 present descriptive statistical summaries for stress values under tension and compression processes, respectively. Both datasets contain 11,158 observations with nearly identical mean values

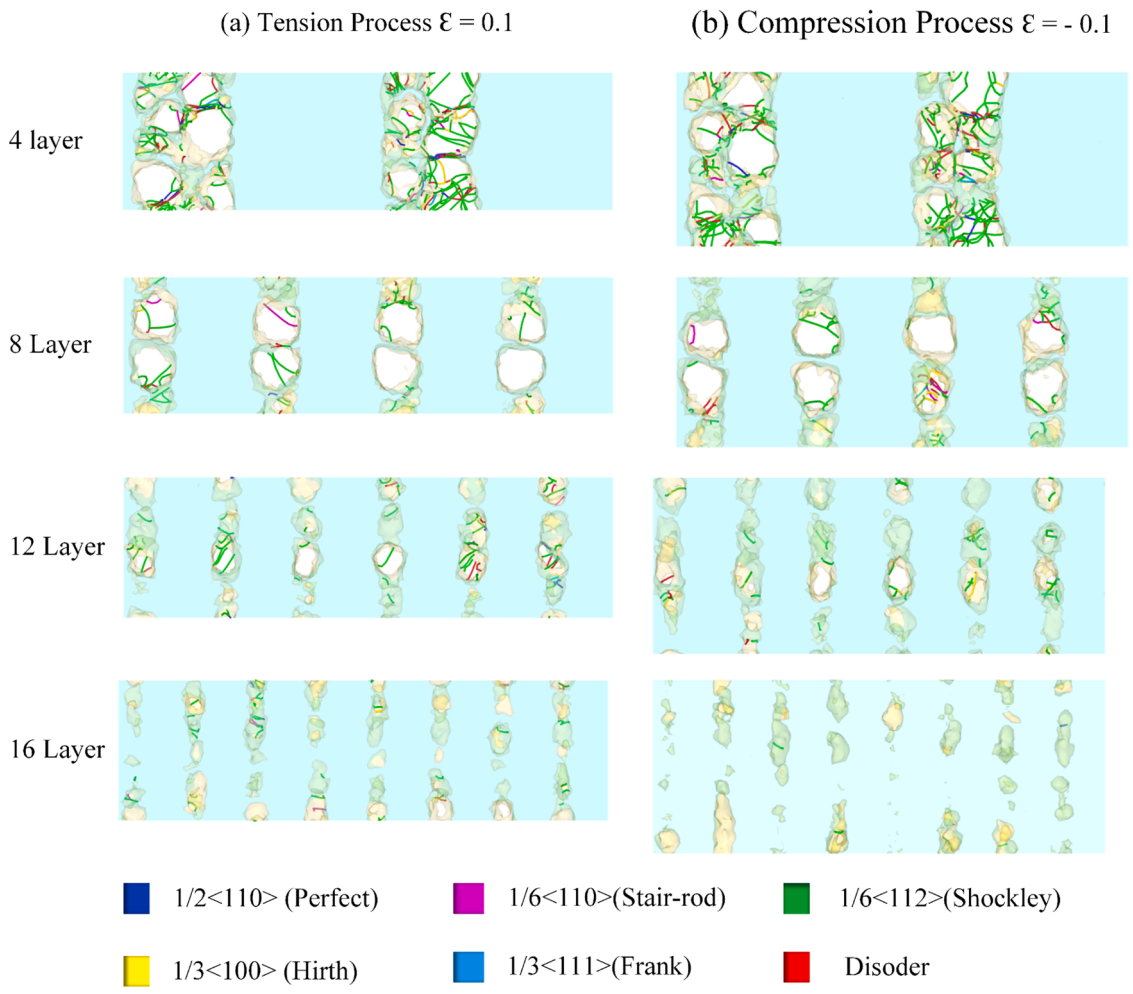

Fig. 15. The dislocation distribution under the tension and compression at a strain rate of 10^9 s^{-1} and 300 K with various layer numbers.

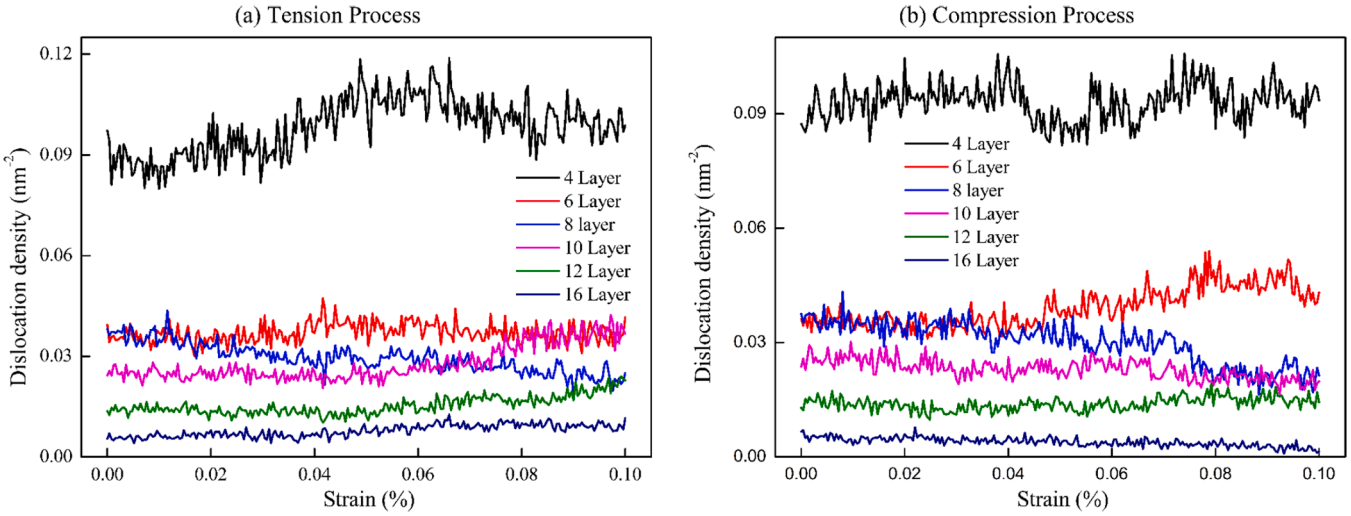

Fig. 16. Evolutions of dislocation densities under the tension and compression processes at 300 K and strain rates of 10^9 s^{-1} with different layer numbers.

for layer, temperature, strain rate, and strain across the two processes. The mean tension stress is higher, at 2.03 GPa, compared to the mean compression stress of 1.29 GPa. While the standard deviation is also more significant for tension stress (1.19 GPa), the compression stress shows a more constrained variation with a standard deviation of 0.56 GPa. The maximum tension stress reaches 5.97 GPa, while the maximum compression stress is capped at 3.85 GPa.

Tables 3 and 4 provide a descriptive statistical analysis of dislocation values under tension and compression processes. Both datasets contain 5588 observations, with similar mean values for layer, temperature,

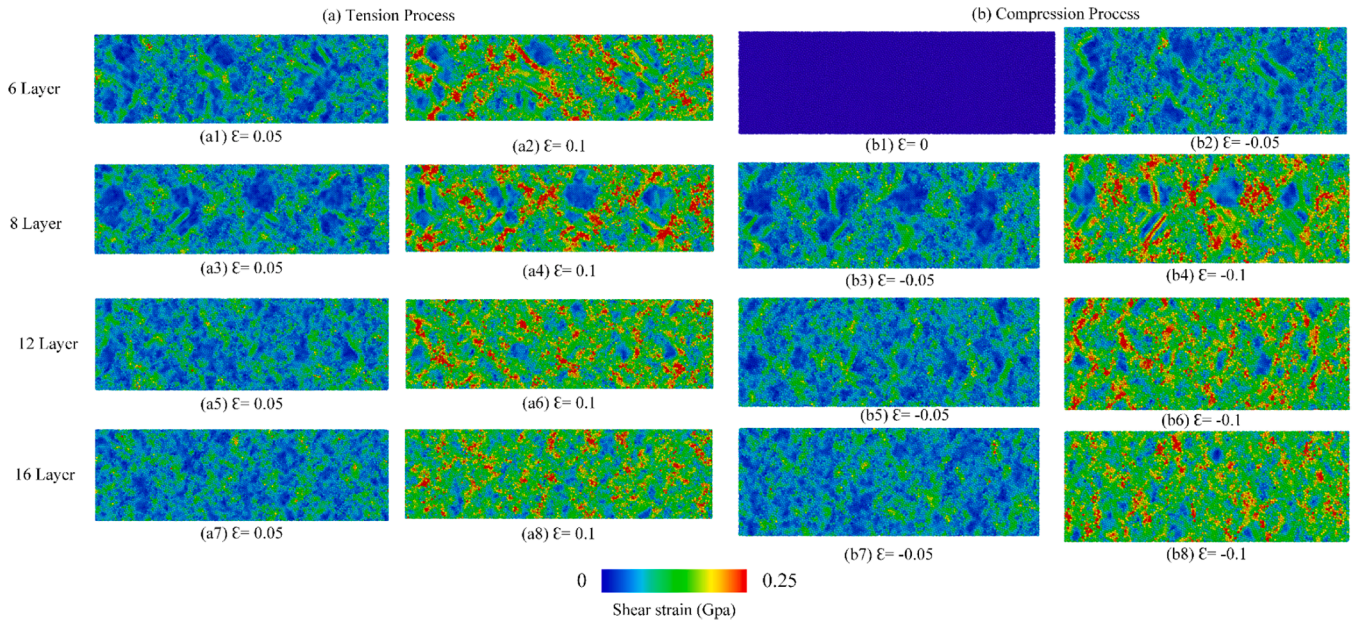

Fig. 17. Shear strain distribution under the tension and compression process at 300 K and strain rates at 10^9 s^{-1} with different layer numbers.

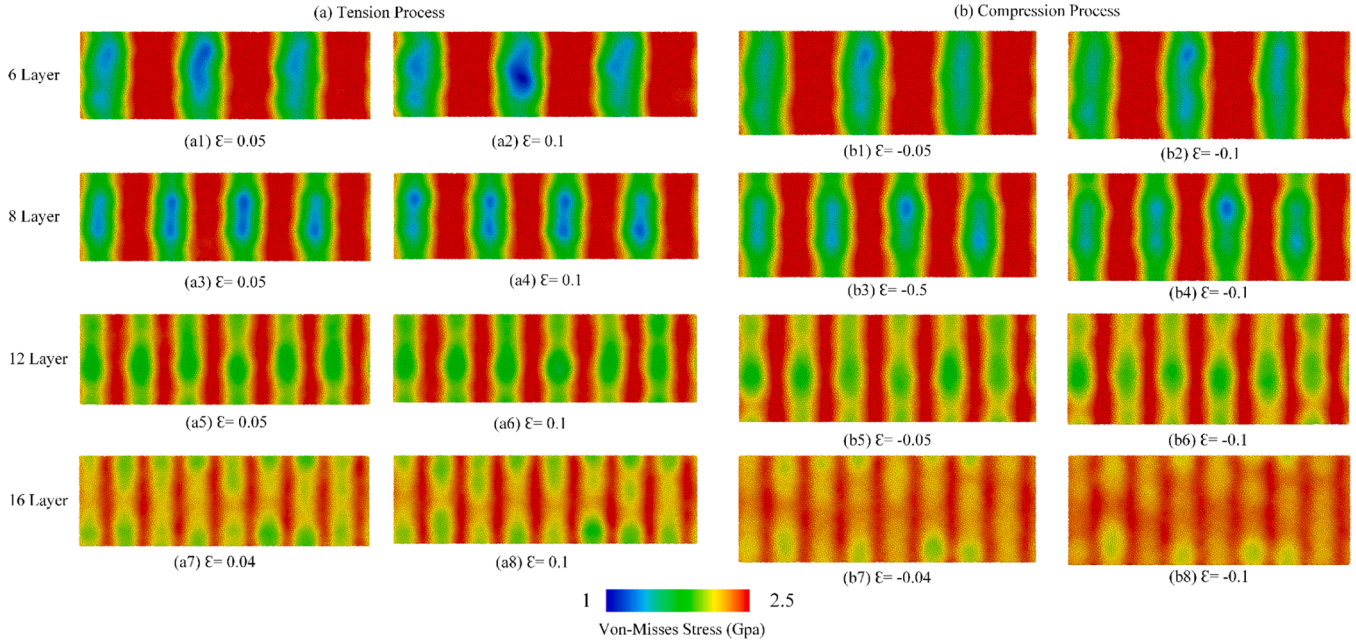

Fig. 18. The von Mises stress distribution of Cu/Zr MNFs under tension and compression at 300 K and strain rate of 10^9 s^{-1} with various layer numbers.

Table 1
Descriptive Statistical Exploratory Data Analysis for Stress Values Under Tension Process.

	Layer	Temperature (K)	Strain rate (s^{-1})	Strain	Tension Stress (GPa)
Count	11,158	11,158	11,158	11,158	11,158
Mean	5.436279	322.04554	6.291092×10^{8}	5.002689×10^{-2}	2.032002
Std	3.128656	78.88617	8.735179×10^{8}	2.888962×10^{-2}	1.88172
Min	4.0	200.0	1.000000×10^{7}	0.0	−0.131507
25 %	4.0	300.0	1.000000×10^{8}	2.500000×10^{-2}	0.984422
50 %	4.0	300.0	5.000000×10^{8}	5.000000×10^{-2}	1.888691
75 %	4.0	600.0	1.000000×10^{9}	7.500000×10^{-2}	3.017215
Max	16.0	600.0	1.000000×10^{10}	0.1	5.966197

Table 2
Descriptive Statistical Exploratory Data Analysis for Stress Values Under Compression Process.

	Layer	Temperature (K)	Strain rate (s^{-1})	Strain	Tension Stress (GPa)
Count	11,158	11,158	11,158	11,158	11,158
Mean	5.433949	322.4592	6.291092×10^{8}	5.002689×10^{-2}	1.294517
Std	3.126459	78.9340	8.735179×10^{8}	2.888962×10^{-2}	0.561162
Min	4.0	200.0	1.000000×10^{7}	0.0	0
25 %	4.0	300.0	1.000000×10^{8}	2.500000×10^{-2}	0.921947
50 %	4.0	300.0	5.000000×10^{8}	5.000000×10^{-2}	1.147656
75 %	4.0	600.0	1.000000×10^{9}	7.500000×10^{-2}	1.788138
Max	16.0	600.0	1.000000×10^{10}	0.1	3.851015

Table 3
Descriptive Statistical Exploratory Data Analysis for Dislocation Values Under Tension Process.

	Layer	Temperature (K)	Strain rate (s^{-1})	Strain	Tension Stress (GPa)
Count	5588	5588	5588	5588	5588
Mean	5.437366	322.4767	6.307445×10^{8}	5.000895×10^{-2}	0.023081
Std	3.129537	78.94159	8.784289×10^{8}	2.893771×10^{-2}	0.026863
Min	4.0	200.0	1.000000×10^{7}	0.0	0.0
25 %	4.0	300.0	1.000000×10^{8}	2.491000×10^{-2}	0.00517
50 %	4.0	300.0	5.000000×10^{8}	5.000000×10^{-2}	0.010595
75 %	4.0	600.0	1.000000×10^{9}	7.513000×10^{-2}	0.035085
Max	16.0	600.0	1.000000×10^{10}	0.1	0.15849

Table 4
Descriptive Statistical Exploratory Data Analysis for Dislocation Values Under Compression Process.

	Layer	Temperature (K)	Strain rate (s^{-1})	Strain	Tension Stress (GPa)
Count	5588	5588	5588	5588	5588
Mean	5.437366	322.4767	6.307445×10^{8}	5.000895×10^{-2}	0.013986
Std	3.129537	78.94159	8.784289×10^{8}	2.893771×10^{-2}	0.011615
Min	4.0	200.0	1.000000×10^{7}	0.0	0.0
25 %	4.0	300.0	1.000000×10^{8}	2.491000×10^{-2}	0.005778
50 %	4.0	300.0	5.000000×10^{8}	5.000000×10^{-2}	0.01105
75 %	4.0	600.0	1.000000×10^{9}	7.513000×10^{-2}	0.01886
Max	16.0	600.0	1.000000×10^{10}	0.1	0.13085

strain rate, and strain across the two processes. The mean dislocation value under tension is higher, at 0.0231, compared to the mean dislocation value under compression, which is 0.0140. The standard deviation for tension dislocation is also larger (0.0269), indicating greater variability compared to the compression dislocation's standard deviation of 0.0116. Maximum dislocation values are 0.15849 under tension and 0.13085 under compression.

3.2.2. Experimental setups

Our experimental setup for the discriminative models was executed on powerful GPUs provided by OpenSource Google Colab's cloud service. We implemented the discriminative models using the scikit-learn library and the Keras framework within a Python environment. For the generative model, GPR model, we utilized the gpflow library from TensorFlow [95], ensuring robust implementation of the generative approach. The data for each experiment was split into two sets: 70 % for training and 30 % for evaluation, allowing us to assess the performance of the models.

Building on insights from previous research on optimizing neural network structures, we have implemented strategies to enhance model performance and ensure stability. This includes integrating dropout techniques, with a probability of 0.25, to prevent overfitting by randomly omitting units during training. Additionally, we selected the GlorotNormal initializer due to its effectiveness in maintaining the output variance of a unit proportional to its input variance, thereby optimizing weight initialization. Batch normalization was also employed to accelerate training and improve performance by standardizing inputs at each layer. These hyperparameters were carefully selected and fine-tuned to achieve optimal model performance.

Table 5
Evaluation for Stress Prediction Under Tension.

Evaluation	FFNN	CNN	LSTM	BiLSTM	GRU	RNN	GPR
MAE	0.119	0.131	0.108	0.052	0.099	0.068	1.355
RMSE	0.178	0.189	0.151	0.068	0.145	0.104	1.669
R^2	0.977	0.973	0.984	0.997	0.984	0.992	0.999

3.2.3. Experimental results

Table 5 compares the performance of several machine learning models, both discriminative and generative, using three evaluation metrics. Discriminative learning models include FFNN, CNN, LSTM, BiLSTM, GRU, and RNN, while GPR represents the generative learning approach. Among the discriminative models, BiLSTM achieves the best results with the lowest MAE (0.052) and RMSE (0.068), and the highest R^2 (0.997), indicating it provides the most accurate predictions. Other discriminative models, such as GRU and RNN, perform well with high R^2 values (0.984 and 0.992, respectively) but outperform BiLSTM regarding error metrics. GPR, the generative model, demonstrates the highest R^2 (0.999), suggesting it effectively captures the overall variance in the data, though it has higher prediction errors (MAE of 1.355 and

Table 6
Evaluation for Stress Prediction Under Compression.

Evaluation	FFNN	CNN	LSTM	BiLSTM	GRU	RNN	GPR
MAE	0.131	0.137	0.095	0.058	0.141	0.072	0.628
RMSE	0.178	0.192	0.129	0.079	0.211	0.097	0.791
R^2	0.880	0.863	0.944	0.980	0.849	0.969	0.977

RMSE of 1.669) compared to the discriminative models. Overall, BiLSTM stands out as the most accurate model for prediction, while GPR excels in explaining data variability.

Table 6 presents the performance evaluation of various models for stress prediction under compression using three key metrics. Among the discriminative models, BiLSTM demonstrates the best overall performance, with the lowest MAE (0.058) and RMSE (0.079) and the highest R^2 (0.980), indicating high accuracy and low prediction errors.

Other models, such as LSTM and RNN, also show strong results, with RNN achieving an R^2 of 0.969 and LSTM achieving an R^2 of 0.944, but their error metrics are slightly higher than BiLSTM. The GPR model, while showing a substantial R^2 value of 0.977, has significantly higher MAE (0.628) and RMSE (0.791), suggesting that while it explains a good portion of the variance in the data, its predictions are less precise compared to the discriminative models. Overall, BiLSTM outperforms the other models in terms of accuracy and variance explanation for stress prediction under compression.

Table 7 compares the performance of the BiLSTM and GPR models using three evaluation metrics. The BiLSTM model exhibits a lower MAE (0.0038) and RMSE (0.005), indicating more precise predictions with minor errors. However, the GPR model achieves a higher R^2 value (0.983), which suggests that it explains more variance in the data compared to BiLSTM despite having higher error values (MAE of 0.0255 and RMSE of 0.0377). This indicates that while BiLSTM provides more accurate predictions on an individual level, the GPR model is better at capturing the overall trends and variance within the dataset.

Table 8 compares the performance of the BiLSTM and Gaussian Process Regression (GPR) models based on three key metrics. The BiLSTM model has lower MAE (0.0038) and RMSE (0.004), indicating more precise predictions with smaller errors. However, GPR performs better in terms of R^2 (0.9), meaning it explains a higher proportion of the variance in the data compared to BiLSTM, which has an R^2 of 0.799. This suggests that while BiLSTM may be better at making accurate point predictions, GPR captures the overall trends and variability in the dataset more effectively. In summary, BiLSTM is preferable for precise predictions, while GPR excels in modeling the general structure of the data.

The evaluation results from the four tables demonstrate several key insights regarding the performance of discriminative learning (BiLSTM) and generative learning (GPR) models for stress and dislocation density prediction. When trained on larger datasets, such as in the stress prediction (Table 5 and Table 6), both BiLSTM and GPR perform well based on the evaluation metrics (MAE, RMSE, and R^2). However, the discriminative learning model, BiLSTM, slightly outperforms GPR in terms of accuracy, achieving lower MAE and RMSE values, particularly under the tension process. BiLSTM's precise predictions and high R^2 value indicate it can provide more accurate point estimates.

In contrast, when trained on smaller datasets, such as in the dislocation prediction (Tables 7 and 8), there is a noticeable decrease in BiLSTM's performance. The MAE and RMSE values increase, and the R^2 value drops, suggesting that BiLSTM struggles more with smaller datasets. Meanwhile, the GPR model maintains strong performance across large and small datasets, with consistently high R^2 values, even though its error metrics (MAE and RMSE) are generally more extensive than those of BiLSTM.

Overall, the results across the four tables suggest that while BiLSTM is highly effective for point prediction and accuracy on larger datasets, the GPR model is more reliable when explaining the overall variance in the data, as reflected by its higher R^2 values in all cases. GPR excels at capturing the underlying data structure and variability, making it a robust choice, especially for smaller datasets where discriminative models like BiLSTM may experience a more significant drop in performance.

Table 7
Evaluation for Dislocation Density Prediction Under Tension.

Evaluation	BiLSTM	GPR
MAE	0.0038	0.0255
RMSE	0.005	0.0377
R^2	0.962	0.983

Table 8
Evaluation for Dislocation Density Prediction Under Compression.

Evaluation	BiLSTM	GPR
MAE	0.0038	0.011
RMSE	0.004	0.015
R^2	0.799	0.9

The experiment results from Fig. 19 and Fig. 20 for the GPR model are illustrated through scatter plots comparing the predicted and actual values for both stress and dislocation density under tension and compression processes. For stress prediction, the plots show a strong correlation between the predicted and actual values, with data points aligning closely along the diagonal, especially for lower stress values. While the GPR model performs accurately overall, slight deviations and outliers appear as the stress values increase, particularly in the compression process. Similarly, for dislocation density predictions, the model captures the general trend well, with most points closely following the diagonal line. However, the compression dislocation plot reveals more deviations at higher dislocation values. Despite these minor discrepancies, the GPR model excels in explaining the overall variance in both stress and dislocation predictions, demonstrating its effectiveness in capturing data trends and variability across both tension and compression processes.

Evaluating discriminative (BiLSTM) and generative (GPR) models across stress and dislocation density prediction tasks demonstrates distinct strengths and weaknesses depending on dataset size and prediction accuracy requirements. When trained on larger datasets, such as stress prediction tasks, the BiLSTM model consistently achieves lower error metrics (MAE, RMSE) and high R^2 values, indicating its superior ability to provide precise point predictions. However, when applied to smaller datasets, such as dislocation density prediction, BiLSTM shows a noticeable performance drop, with increased errors and reduced R^2 values. This suggests that BiLSTM's performance is more sensitive to data size and may struggle when fewer training samples are available. On the other hand, the GPR model shows a remarkable ability to maintain strong performance across large and small datasets. Although its MAE and RMSE values are generally higher than those of BiLSTM, GPR consistently delivers high R^2 values, suggesting that it excels in capturing the overall variance and underlying trends in the data. This characteristic makes GPR more reliable for understanding data structure and variability, especially in scenarios where accurate point predictions are not the sole priority. The scatter plots from Fig. 19 and Fig. 20 further illustrate GPR's strengths. For both stress and dislocation density predictions under tension and compression, the GPR model shows a strong correlation between predicted and actual values, aligning closely with the ideal diagonal line. While there are minor deviations and outliers, particularly in the compression process, the GPR model demonstrates its robustness in capturing the overall patterns in the dataset.

Research on Cu/Zr metallic nanofibers (MNFs) has generated extensive data on their mechanical properties under tension-compression testing, contributing to a comprehensive understanding of these materials. This study distinguishes itself from prior research by incorporating tension-compression deformation into its models. Data analysis reveals that the tensile and compressive strengths predicted in this study are in good agreement with the experimental findings reported by Pal et al. [51] and Hussain et al. [86]. Furthermore, while the thermal conditions and deformation rates employed in our MD simulations are lower than those used by Tran et al. [90], they are comparable to the experimental setups described by Wang et al. [19] and Nakamura et al. [45]. Table 9 presents a summary of the mechanical properties

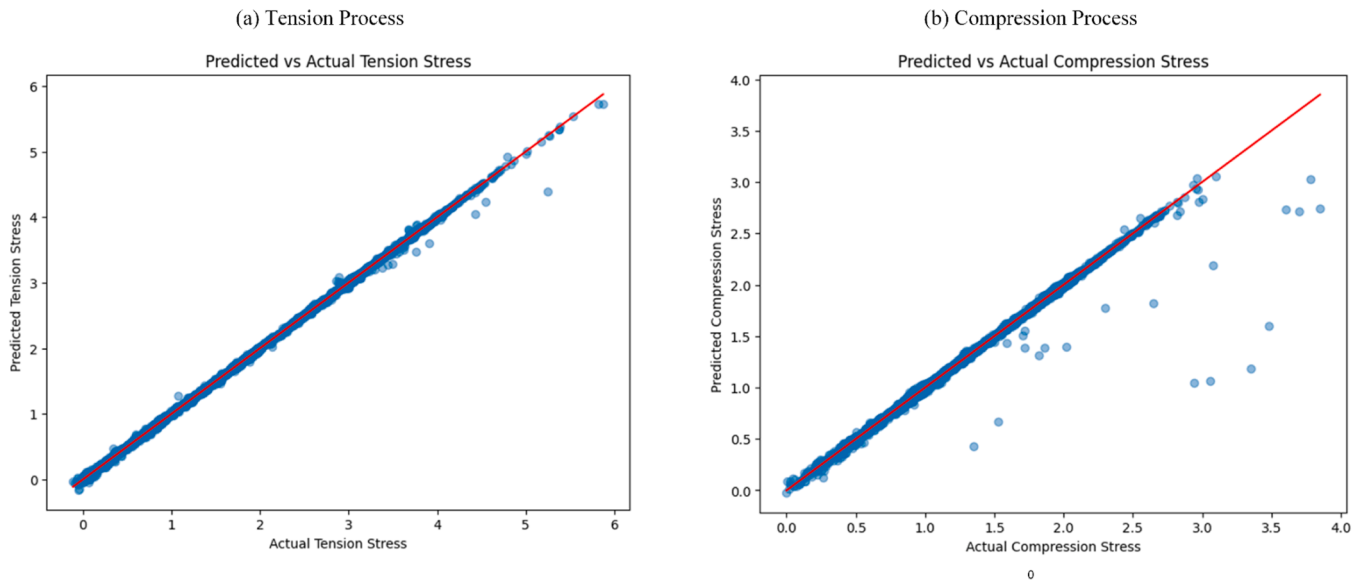

Fig. 19. Stress prediction under tension and compression process from the GPR model.

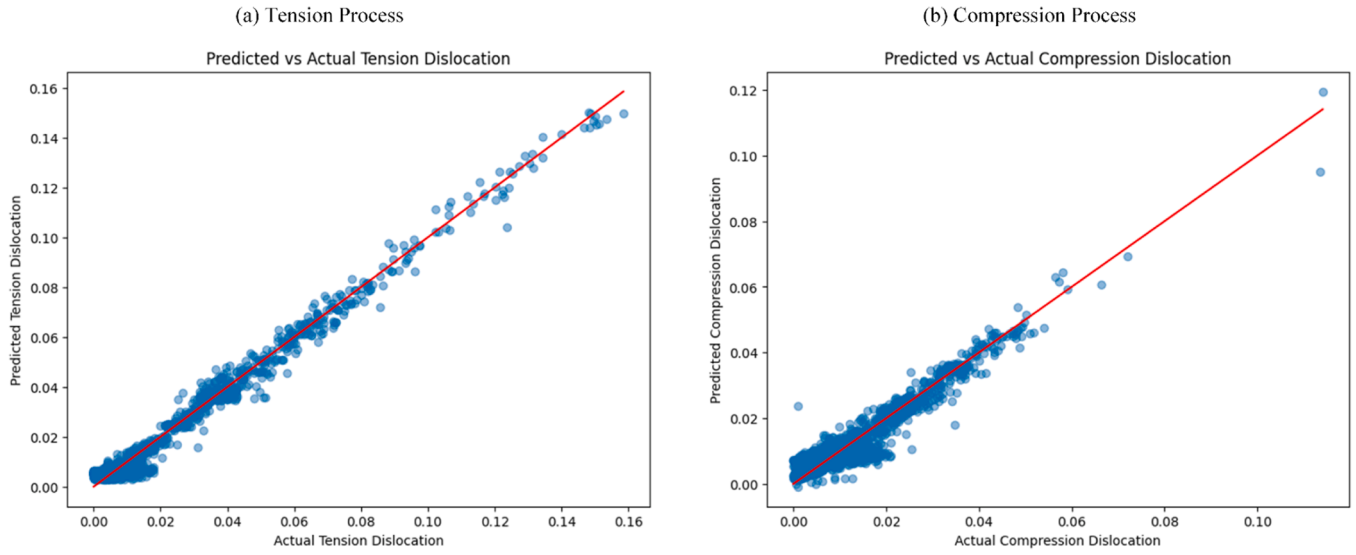

Fig. 20. Dislocation prediction under tension and compression process from the GPR model.

Table 9
The comparison of several parameters between investigations using MD simulation and experimental.

Material	Strain rate (s^{-1})	Temperature (K)	Strain (%)	Stress (GPa)	Layer number	Method	Reference
CuZr	10^8 - 10^{10}	200 - 600	± 10	1.5 - 5.97	4 - 16	MD and ML	This study
Cu/CuZr	1.25× 10^8	50	16.9	3.1–3.24	–	MD Simulation	Song et al. [10]
Cu/Zr	1.25× 10^8	150 - 600	4	6.3–21.05	1 - 20	MD Simulation	Hsu et al. [11]
CuZr	2.3–2.8 × 10^{-6}	–	6.8	0.941–1.22	–	Experimental	Wang et al. [19]
Ni/Co	10^8 - 10^{10}	100 - 700	25	9.1–12.6	2 - 10	MD Simulation	Vu et al. [33]
CuZr	10^{10} - 10^{13}	2000	8	3.1–0.38	–	MD Simulation	Wang et al. [38]
Cu-Zr	2 × 10^8 - 10^9	700	25	1.9 - 3	–	Experimental	Nakamura et al. [45]
Cu-Zr	10^8	100	25	3.5 - 7.5	–	MD Simulation	Pal et al. [51]
CuZr	10^8 - 10^{10}	300	30	1.6 - 2.7	–	MD Simulation	Hussain et al. [86]
Cu/Ta	10^8 - 10^{10}	100 - 900	15	9.5 – 21.15	2 - 10	MD Simulation	Tran et al. [90]

obtained in previous experimental and simulation studies, demonstrating a strong consistency with our results. This alignment supports the validity of our computational approach and provides valuable insights for future investigations into Cu-Zr-based metallic nanocomposites.

4. Conclusions

In summary, we have investigated the influence of various temperatures, strain rates, and layers on the mechanical response of Cu/Zr MNFs under tension-compression loading through MD simulations and

AI. As a result, the following conclusions may be drawn below:

(1) Under identical circumstances, it is observed that the tensile process exhibits a higher yield strength compared to the compressive process.
(2) At equivalent temperature and strain rate conditions, compressive stresses exhibit lower magnitudes of stability compared to tensile stresses as stress levels decline.
(3) Compressive stress demonstrates more minor stability under equivalent temperature and strain rate conditions than tensile stress with decreasing stress levels. Conversely, despite the influence of varying layers, both stresses exhibit minimal variation in the similar.
(4) Elevating the temperature reduces dislocation density, whereby the density of dislocations generated during tensile deformation surpasses that observed during compressive deformation.
(5) The FCC arrangement characteristic of Cu layers undergoes a pronounced transformation towards amorphous, BCC, and HCP structures. Conversely, the HCP structure in Zr layers experiences a minor transition towards the BCC and amorphous configurations. An oblique SF manifests within the Cu layer at the interfacial zone of the Cu/Zr MNFs, propagating into the Cu layers during tension and compression.
(6) The BiLSTM model is highly effective for precise predictions, particularly on larger datasets, making it a strong choice for applications requiring high accuracy in point estimates.
(7) The GPR model stands out because it can generalize across varying dataset sizes and explain data variability.

This study investigated the atomic-level mechanisms governing tension-compression ductility in Cu/Zr MNFs and the evolution of microstructures under tension and compression deformations. However, it is essential to note that in Cu/Zr MNFs featuring grain boundaries (GBs), the impact of diverse conditions and mechanisms may vary, particularly in specimens characterized by larger grain dimensions. Therefore, future investigations are warranted to systematically analyze the cyclic plasticity behavior exhibited by Cu/Zr MNFs. The GPR a more robust model in applications where understanding data trends and capturing overall variance are more critical, particularly for smaller datasets where discriminative models may falter.

CRediT authorship contribution statement

Hoang-Giang Nguyen: Writing – review & editing, Writing – original draft, Visualization, Validation, Software, Data curation, Conceptualization. **Sheng-Joue Young:** Supervision, Software, Resources, Project administration, Methodology, Funding acquisition, Formal analysis. **Thanh-Dung Le:** Writing – review & editing, Writing – original draft, Visualization, Validation, Software, Methodology, Formal analysis, Data curation. **Chi-Ngon Nguyen:** Supervision, Software, Resources, Project administration, Methodology, Funding acquisition. **Le-Binh Do:** Supervision, Resources, Methodology, Investigation, Formal analysis. **Thai-Nam Nguyen:** Writing – review & editing, Investigation, Data curation, Conceptualization. **Te-Hua Fang:** Writing – review & editing, Supervision, Software, Resources, Project administration, Methodology, Funding acquisition.

Declaration of competing interest

The authors declare that they have no known competing financial interests or personal relationships that could have appeared to influence the work reported in this paper.

Acknowledgments

The authors acknowledge the support from the National Science and Technology Council, Taiwan, under grant numbers NSTC 113–2221-E-992–067-MY3, NSTC 113–2811-E239–002, and Industry Cooperation Project no. 113A00262.

References

[1] Y. Zhang, J. Li, Q. Zhang, S. Ding, W. Wu, R. Xia, Tetrachiral nanostructured metallic glasses with mechanically tunable performance, Mater Chem Phys 276 (2022) 125315.
[2] A.S. Tran, Strengthening mechanism and plasticity deformation of crystalline/amorphous Cu/CuTa nanomultilayer, J Non Cryst Solids 559 (2021) 120685.
[3] D. Wang, T. Kups, J. Schawohl, P. Schaaf, Deformation behavior of Au/Ti multilayers under indentation, J. Mater. Sci.: Mater. Electron 23 (2012) 1077–1082.
[4] P.M. Anderson, J.S. Carpenter, Estimates of interfacial properties in Cu/Ni multilayer thin films using hardness data, Scr Mater 62 (6) (2010) 325–328.
[5] R.C. Cammarata, T.E. Schlesinger, C. Kim, S.B. Qadri, A.S. Edelstein, Nanoindentation study of the mechanical properties of copper-nickel multilayered thin films, Appl Phys Lett 56 (19) (1990) 1862–1864.
[6] H. Zhou, X. Mu, W. Zhao, D. Tang, P. Wei, W. Zhu, Q. Zhang, Low interface resistance and excellent anti-oxidation of Al/Cu/Ni multilayer thin-film electrodes for Bi2Te3-based modules, Nano Energy 40 (2017) 274–281.
[7] T. Fu, X. Peng, X. Chen, S. Weng, N. Hu, Q. Li, Z. Wang, Molecular dynamics simulation of nanoindentation on Cu/Ni nanotwinned multilayer films using a spherical indenter, Sci Rep 6 (1) (2016) 35665.
[8] M.Z. Wei, Z.H. Cao, J. Shi, G.J. Pan, L.J. Xu, X.K. Meng, Anomalous plastic deformation in nanoscale Cu/Ta multilayers, Mater. Sci. Eng.: A 598 (2014) 355–359.
[9] H.Y. Song, P. Yin, X.D. Zuo, M.R. An, Y.L. Li, Atomic simulations of plastic deformation mechanism of MgAl/Mg nanoscale amorphous/crystalline multilayers, J Non Cryst Solids 500 (2018) 121–128.
[10] H.Y. Song, J.J. Xu, Y.G. Zhang, S. Li, D.H. Wang, Y.L. Li, Molecular dynamics study of deformation behavior of crystalline Cu/amorphous Cu50Zr50 nanolaminates, Mater Des 127 (2017) 173–182.
[11] K.C. Hsu, J.Y. Chen, T.H. Fang, M.H. Lin, Size-dependent strength and interface-dominated deformation mechanisms of Cu/Zr multilayer nanofilms, Results Phys 11 (2018) 684–689.
[12] S. Weng, H. Ning, N. Hu, C. Yan, T. Fu, X. Peng, L. Wu, Strengthening effects of twin interface in Cu/Ni multilayer thin films–A molecular dynamics study, Mater Des 111 (2016) 1–8.
[13] T. Fu, X. Peng, C. Huang, D. Yin, Q. Li, Z. Wang, Molecular dynamics simulation of VN thin films under indentation, Appl Surf Sci 357 (2015) 643–650.
[14] J.Y. Chen, H.G. Nguyen, M.H. Lin, T.H. Fang, Mechanical and electrochemical characterization of CuAlNi alloys, Curr. Appl. Phys 69 (2025) 8–20.
[15] J. Sarkar, D.K. Das, Nanoindentation study of mechanical behavior and response of a single layer pristine silicene sheet using molecular dynamics simulations, Comput. Mater. Sci 147 (2018) 64–71.
[16] H.G. Nguyen, T.H. Fang, D.Q. Doan, Cyclic plasticity and deformation mechanism of AlCrCuFeNi high entropy alloy, J Alloys Compd 940 (2023) 168838.
[17] Y.Y. Lu, R. Kotoka, J.P. Ligda, B.B. Cao, S.N. Yarmolenko, B.E. Schuster, Q. Wei, The microstructure and mechanical behavior of Mg/Ti multilayers as a function of individual layer thickness, Acta Mater 63 (2014) 216–231.
[18] W.J. Chang, T.H. Fang, Influence of temperature on tensile and fatigue behavior of nanoscale copper using molecular dynamics simulation, J. Phys. Chem. Solids 64 (8) (2003) 1279–1283.
[19] D. Wang, J. Mu, Y. Chen, Y. Qi, W. Wu, Y. Wang, K. An, A study of stress-induced phase transformation and micromechanical behavior of CuZr-based alloy by in-situ neutron diffraction, J Alloys Compd 696 (2017) 1096–1104.
[20] J. Luo, K. Dahmen, P.K. Liaw, Y. Shi, Low-cycle fatigue of metallic glass nanowires, Acta Mater 87 (2015) 225–232.
[21] T. Zientarski, D. Chocyk, Structure and stress in Cu/Au and Fe/Au systems: a molecular dynamics study, Thin Solid Films 562 (2014) 347–352.
[22] D.V. Louzguine-Luzgin, V.Y. Zadorozhnyy, S.V. Ketov, Z. Wang, A.A. Tsarkov, A. L. Greer, On room-temperature quasi-elastic mechanical behaviour of bulk metallic glasses, Acta Mater 129 (2017) 343–351.
[23] D.Q. Doan, T.H. Fang, A.S. Tran, T.H. Chen, Residual stress and elastic recovery of imprinted Cu-Zr metallic glass films using molecular dynamic simulation, Comput. Mater. Sci 170 (2019) 109162.
[24] Y.R. Jeng, C.M. Tan, Investigation into the nanoindentation size effect using static atomistic simulations, Appl Phys Lett 89 (25) (2006).
[25] T. Fu, X. Peng, C. Wan, Z. Lin, X. Chen, N. Hu, Z. Wang, Molecular dynamics simulation of plasticity in VN (001) crystals under nanoindentation with a spherical indenter, Appl Surf Sci 392 (2017) 942–949.
[26] D.Q. Doan, T.H. Fang, T.H. Chen, Influences of grain size and temperature on tribological characteristics of CuAlNi alloys under nanoindentation and nanoscratch, Int. J. Mech. Sci 185 (2020) 105865.
[27] H.G. Nguyen, T.H. Fang, Machining mechanism and residual stress of AlCuCrFeNi alloy, Int. J. Mech. Sci (2024) 109429.
[28] T.X. Bui, T.H. Fang, C.I. Lee, Strain rate and shear-transformation zone response of nanoindentation and nanoscratching on Ni50Zr50 metallic glasses using molecular dynamics, Phys. B: Condens. Matter 583 (2020) 412021.
[29] S. Li, P. Huang, F. Wang, Achieving pronounced β-relaxations and improved plasticity in CuZr metallic glass, J Alloys Compd 850 (2021) 156774.

[30] M.A. Tschopp, G.J. Tucker, D.L. McDowell, Atomistic simulations of tension–compression asymmetry in dislocation nucleation for copper grain boundaries, Comput. Mater. Sci 44 (2) (2008) 351–362.
[31] X.L. Wang, F. Jiang, H. Hahn, J. Li, H. Gleiter, J. Sun, J.X. Fang, Plasticity of a scandium-based nanoglass, Scr Mater 98 (2015) 40–43.
[32] Y.R. Jeng, P.C. Tsai, T.H. Fang, Molecular dynamics investigation of the mechanical properties of gallium nitride nanotubes under tension and fatigue, Nanotechnology 15 (12) (2004) 1737.
[33] T.N. Vu, V.T. Pham, V.T. Nguyen, T.H. Fang, Interfacial strength and deformation mechanism of Ni/Co multilayers under uniaxial tension using molecular dynamics simulation, Mater. Today Commun 30 (2022) 103088.
[34] H.G. Nguyen, T.H. Fang, Mechanics of AlCuNiTi alloy orthogonal micro-cutting, Model. Simul. Mater. Sci. Eng 31 (8) (2023) 085016.
[35] D.Q. Doan, T.H. Fang, T.H. Chen, Machining mechanism and deformation behavior of high-entropy alloy under elliptical vibration cutting, Intermetallics 131 (2021) 107079.
[36] Y. Bai, C. She, Atomic structure evolution in metallic glasses under cyclic deformation, Comput. Mater. Sci 169 (2019) 109094.
[37] A.D. Anggono, M.Z. Mahmoud, W. Suksatan, S. Chupradit, M.H. Ali, Y.F. Mustafa, A. Surendar, Combined effects of annealing and cyclic loading on structural rejuvenation and mechanical properties of CuZr metallic glass: a molecular dynamics study, Mater. Res 25 (2022) e20210494.
[38] P. Wang, X. Yang, Atomistic investigation of aging and rejuvenation in CuZr metallic glass under cyclic loading, Comput. Mater. Sci 185 (2020) 109965.
[39] X.D. Wang, R.T. Qu, S.J. Wu, Z.Q. Liu, Z.F. Zhang, Fatigue damage and fracture behavior of metallic glass under cyclic compression, Mater. Sci. Eng.: A 717 (2018) 41–47.
[40] C.M. Meylan, F. Papparotto, S. Nachum, J. Orava, M. Miglierini, V. Basykh, A. L. Greer, Stimulation of shear-transformation zones in metallic glasses by cryogenic thermal cycling, J Non Cryst Solids 548 (2020) 120299.
[41] N.V. Priezjev, The effect of cryogenic thermal cycling on aging, rejuvenation, and mechanical properties of metallic glasses, J Non Cryst Solids 503 (2019) 131–138.
[42] M. Sepúlveda-Macías, N. Amigo, G. Gutiérrez, Onset of plasticity and its relation to atomic structure in CuZr metallic glass nanowire: a molecular dynamics study, J Alloys Compd 655 (2016) 357–363.
[43] J. Li, J. Guo, H. Luo, Q. Fang, H. Wu, L. Zhang, Y. Liu, Study of nanoindentation mechanical response of nanocrystalline structures using molecular dynamics simulations, Appl Surf Sci 364 (2016) 190–200.
[44] S.S. Jiang, Y.J. Huang, F.F. Wu, P. Xue, J.F. Sun, A CuZr-based bulk metallic glass composite with excellent mechanical properties by optimizing microstructure, J Non Cryst Solids 483 (2018) 94–98.
[45] A. Nakamura, Y. Kamimura, K. Edagawa, S. Takeuchi, Elastic and plastic characteristics of a model Cu–Zr amorphous alloy, Mater. Sci. Eng.: A 614 (2014) 16–26.
[46] Z. Ning, W. Liang, M. Zhang, Z. Li, H. Sun, A. Liu, J. Sun, High tensile plasticity and strength of a CuZr-based bulk metallic glass composite, Mater Des 90 (2016) 145–150.
[47] P. Xue, S. Pauly, W. Gan, S. Jiang, H. Fan, Z. Ning, J. Sun, Enhanced tensile plasticity of a CuZr-based bulk metallic glass composite induced by ion irradiation, J. mater. sci. technol 35 (10) (2019) 2221–2226.
[48] D.Y. Wu, K.K. Song, P. Gargarella, C.D. Cao, R. Li, I. Kaban, J. Eckert, Glass-forming ability, thermal stability of B2 CuZr phase, and crystallization kinetics for rapidly solidified Cu–Zr–Zn alloys, J Alloys Compd 664 (2016) 99–108.
[49] J.J. Niu, J.Y. Zhang, G. Liu, P. Zhang, S.Y. Lei, G.J. Zhang, J. Sun, Size-dependent deformation mechanisms and strain-rate sensitivity in nanostructured Cu/X (X= Cr, Zr) multilayer films, Acta Mater 60 (9) (2012) 3677–3689.
[50] Y.H. Zhu, S.F. Ge, H. Li, A.M. Wang, H.F. Zhang, Z.W. Zhu, Developing in-situ Zr-based bulk metallic glass composites from multi-cluster competition strategy, J Alloys Compd 856 (2021) 158149.
[51] S. Pal, K.V. Reddy, C. Deng, On the role of Cu-Zr amorphous intergranular films on crack growth retardation in nanocrystalline Cu during monotonic and cyclic loading conditions, Comput. Mater. Sci 169 (2019) 109122.
[52] H.G. Nguyen, M.J. Wu, T.H. Fang, Study on copper-to-copper bonding of three-dimensional integrated circuits using the quasicontinuum method, Phys. Scr 99 (6) (2024) 065114.
[53] T.T.B. Ngo, V.T. Nguyen, T.H. Fang, Study of nanoindentation behavior of NiCrCoAl medium entropy alloys under indentation process using molecular dynamics, Model. Simul. Mater. Sci. Eng 32 (3) (2024) 035003.
[54] T.T.B. Ngo, V.T. Nguyen, T.H. Fang, Nanoscale friction behavior and deformation during copper chemical mechanical polishing process, J Mol Model 29 (9) (2023) 293.
[55] C. Zhong, H. Zhang, Q.P. Cao, X.D. Wang, D.X. Zhang, J.W. Hu, J.Z. Jiang, Non-localized deformation in CuZr multi-layer amorphous films under tension, J Alloys Compd 678 (2016) 410–420.
[56] Y.L. Guan, L.S. Dai, J.L. Shao, W.D. Song, Molecular dynamics study on the nanovoid collapse and local deformation in shocked Cu50Zr50 metallic glasses, J Non Cryst Solids 559 (2021) 120703.
[57] T.D. Le, R. Noumeir, H.L. Quach, J.H. Kim, J.H. Kim, H.M. Kim, Critical temperature prediction for a superconductor: a variational bayesian neural network approach, IEEE Trans. Appl. Supercond 30 (4) (2020) 1–5.
[58] J.F. Masson, J.S. Biggins, E. Ringe, Machine learning for nanoplasmonics, Nat Nanotechnol 18 (2) (2023) 111–123.
[59] H.G. Nguyen, T.D. Le, H.G. Nguyen, T.H. Fang, Mechanical properties of AlCoCrCuFeNi high-entropy alloys using molecular dynamics and machine learning, Mater. Sci. Eng.: R: Rep 160 (2024) 100833.
[60] D.Q. Doan, T.H. Fang, T.H. Chen, T.X. Bui, Effects of void and inclusion sizes on mechanical response and failure mechanism of AlCrCuFeNi2 high-entropy alloy, Eng Fract Mech 252 (2021) 107848.
[61] J. Li, Q. Fang, B. Liu, Y. Liu, Y. Liu, Atomic-scale analysis of nanoindentation behavior of high-entropy alloy, J. Micromech. Mol. Phys 1 (01) (2016) 1650001.
[62] C.D. Wu, C.J. Hou, Molecular dynamics analysis of plastic deformation and mechanics of imprinted metallic glass films, Comput. Mater. Sci 144 (2018) 248–255.
[63] C. Qiu, P. Zhu, F. Fang, D. Yuan, X. Shen, Study of nanoindentation behavior of amorphous alloy using molecular dynamics, Appl Surf Sci 305 (2014) 101–110.
[64] F.F. Abraham, Computational statistical mechanics methodology, applications and supercomputing, Adv Phys 35 (1) (1986) 1–111.
[65] M.S. Daw, S.M. Foiles, M.I. Baskes, The embedded-atom method: a review of theory and applications, Mater. Sci. Rep 9 (7–8) (1993) 251–310.
[66] M.I. Mendelev, D.J. Sordelet, M.J. Kramer, Using atomistic computer simulations to analyze x-ray diffraction data from metallic glasses, J Appl Phys 102 (4) (2007).
[67] M.I. Mendelev, M.J. Kramer, R.T. Ott, D.J. Sordelet, D. Yagodin, P.J.P.M. Popel, Development of suitable interatomic potentials for simulation of liquid and amorphous Cu–Zr alloys, Philos. Mag 89 (11) (2009) 967–987.
[68] A. Stukowski, Structure identification methods for atomistic simulations of crystalline materials, Model. Simul. Mater. Sci. Eng 20 (4) (2012) 045021.
[69] A. Stukowski, Visualization and analysis of atomistic simulation data with OVITO–the Open Visualization Tool, Model. simul. mater. sci. eng 18 (1) (2009) 015012.
[70] H. Tsuzuki, P.S. Branicio, J.P. Rino, Structural characterization of deformed crystals by analysis of common atomic neighborhood, Comput Phys Commun 177 (6) (2007) 518–523.
[71] A. Stukowski, K. Albe, Extracting dislocations and non-dislocation crystal defects from atomistic simulation data, Model. Simul. Mater. Sci. Eng 18 (8) (2010) 085001.
[72] A. Stukowski, V.V. Bulatov, A. Arsenlis, Automated identification and indexing of dislocations in crystal interfaces, Model. Simul. Mater. Sci. Eng 20 (8) (2012) 085007.
[73] J. Wang, An intuitive tutorial to Gaussian processes regression, Comput Sci Eng (2023).
[74] V.L. Deringer, A.P. Bartók, N. Bernstein, D.M. Wilkins, M. Ceriotti, G. Csányi, Gaussian process regression for materials and molecules, Chem. Rev 121 (16) (2021) 10073–10141.
[75] E. Schulz, M. Speekenbrink, A. Krause, A tutorial on Gaussian process regression: modelling, exploring, and exploiting functions, J Math Psychol 85 (2018) 1–16.
[76] J. Shi, J. Yang, J. Zhou, H. Ji, X. Tang, T. Gao, Effect of graphene on thermal stability and mechanical properties of ethylene-vinyl acetate: a molecular dynamics simulation, Mater. Res. Express 7 (3) (2020) 035304.
[77] F. Nabarro, Dislocations in a simple cubic lattice, Proc. Phys. Soc 59 (2) (1947) 256.
[78] Y.Y. Zhao, T.G. Nieh, Correlation between lattice distortion and friction stress in Ni-based equiatomic alloys, Intermetallics 86 (2017) 45–50.
[79] H.D. Dietze, Die temperaturabhängigkeit der versetzungsstruktur, Z. fuer Phys 132 (1) (1952) 107–110.
[80] Z. Wu, H. Bei, G.M. Pharr, E.P. George, Temperature dependence of the mechanical properties of equiatomic solid solution alloys with face-centered cubic crystal structures, Acta Mater 81 (2014) 428–441.
[81] S. Jiang, H. Zhang, Y. Zheng, Z. Chen, Atomistic study of the mechanical response of copper nanowires under torsion, J Phys D Appl Phys 42 (13) (2009) 135408.
[82] K. Zhou, B. Liu, S. Shao, Y. Yao, Molecular dynamics simulations of tension–compression asymmetry in nanocrystalline copper, Phys. Lett. A 381 (13) (2017) 1163–1168.
[83] Z. Yang, G. Zhang, J. Zhao, Molecular dynamics simulations of void effect of the copper nanocubes under triaxial tensions, Phys. Lett. A 380 (7–8) (2016) 917–922.
[84] D.Q. Doan, T.H. Fang, T.H. Chen, Nanotribological characteristics and strain hardening of amorphous Cu64Zr36/crystalline Cu nanolaminates, Tribol Int 147 (2020) 106275.
[85] H. Zhou, S. Qu, W. Yang, An atomistic investigation of structural evolution in metallic glass matrix composites, Int. J. Plast 44 (2013) 147–160.
[86] F. Hussain, M. Imran, M. Rashid, H. Ullah, A. Shakoor, E. Ahmad, S.A. Ahmad, Molecular dynamics simulation of mechanical characteristics of CuZr bulk metallic glasses using uni-axial tensile loading technique, Phys. Scr 89 (11) (2014) 115701.
[87] G.P. Potirniche, M.F. Horstemeyer, G.J. Wagner, P.M. Gullett, A molecular dynamics study of void growth and coalescence in single crystal nickel, Int. J. Plast 22 (2) (2006) 257–278.
[88] L. Lu, C. Huang, W. Pi, H. Xiang, F. Gao, T. Fu, X. Peng, Molecular dynamics simulation of effects of interface imperfections and modulation periods on Cu/Ta multilayers, Comput. Mater. Sci 143 (2018) 63–70.
[89] D. Li, F. Wang, Z. Yang, Y. Zhao, How to identify dislocations in molecular dynamics simulations? Sci. China Phys. Mech. Astron 57 (2014) 2177–2187.
[90] A.S. Tran, Phase transformation and interface fracture of Cu/Ta multilayers: a molecular dynamics study, Eng Fract Mech 239 (2020) 107292.
[91] T. Waitz, H.P. Karnthaler, The fcc to hcp martensitic phase transformation in CoNi studied by TEM and AFM methods, Acta Mater 45 (2) (1997) 837–847.
[92] J.H. Yang, C.M. Wayman, Self-accomodation and shape memory mechanism of ϵ-martensite—I. Experimental observations, Mater Charact 28 (1) (1992) 23–35.

[93] D. Zhang, S. Chaudhuri, Solidification dynamics and microstructure evolution in nanocrystalline cobalt, Comput. Mater. Sci 160 (2019) 222–232.
[94] B. Deng, J. Luo, J.T. Harris, C.M. Smith, M.E. McKenzie, Molecular dynamics simulations on fracture toughness of Al2O3-SiO2 glass-ceramics, Scr Mater 162 (2019) 277–280.
[95] A.G.D.G. Matthews, M. Van Der Wilk, T. Nickson, K. Fujii, A. Boukouvalas, P. Le, J. Hensman, GPflow: a Gaussian process library using TensorFlow, J. Mach. Learn. Res 18 (40) (2017) 1–6.